Laser and Particle Beams (2004), *22*, 221–244. Printed in the USA.

DOI: 10.1017/S0263034604223059

Characterization of a bright, tunable, ultrafast Compton scattering X-ray source

F.V. HARTEMANN,[1] A.M. TREMAINE,[1] S.G. ANDERSON,[1] C.P.J. BARTY,[1] S.M. BETTS,[1] R. BOOTH,[1] W.J. BROWN,[1] J.K. CRANE,[1] R.R. CROSS,[1] D.J. GIBSON,[1] D.N. FITTINGHOFF,[1] J. KUBA,[1] G.P. LE SAGE,[1] D.R. SLAUGHTER,[1] A.J. WOOTTON,[1] E.P. HARTOUNI,[1] P.T. SPRINGER,[1] J.B. ROSENZWEIG,[2] AND A.K. KERMAN[3]

[1]Lawrence Livermore National Laboratory, Livermore, CA
[2]University of California at Los Angeles, Department of Physics and Astronomy, Los Angeles, CA
[3]Massachusetts Institute of Technology, Physics Department, Cambridge, MA

(RECEIVED 1 November 2003; ACCEPTED 26 January 2004)

Abstract

The Compton scattering of a terawatt-class, femtosecond laser pulse by a high-brightness, relativistic electron beam has been demonstrated as a viable approach toward compact, tunable sources of bright, femtosecond, hard X-ray flashes. The main focus of this article is a detailed description of such a novel X-ray source, namely the PLEIADES (Picosecond Laser–Electron Inter-Action for the Dynamical Evaluation of Structures) facility at Lawrence Livermore National Laboratory. PLEIADES has produced first light at 70 keV, thus enabling critical applications, such as advanced backlighting for the National Ignition Facility and *in situ* time-resolved studies of high-Z materials. To date, the electron beam has been focused down to $\sigma_x = \sigma_y = 27$ μm rms, at 57 MeV, with 266 pC of charge, a relative energy spread of 0.2%, a normalized horizontal emittance of 3.5 mm·mrad, a normalized vertical emittance of 11 mm·mrad, and a duration of 3 ps rms. The compressed laser pulse energy at focus is 480 mJ, the pulse duration 54 fs Intensity Full Width at Half-Maximum (IFWHM), and the $1/e^2$ radius 36 μm. Initial X rays produced by head-on collisions between the laser and electron beams at a repetition rate of 10 Hz were captured with a cooled CCD using a CsI scintillator; the peak photon energy was approximately 78 keV, and the observed angular distribution was found to agree very well with three-dimensional codes. The current X-ray dose is 3×10^6 photons per pulse, and the inferred peak brightness exceeds 10^{15} photons/(mm^2 × mrad^2 × s × 0.1% bandwidth). Spectral measurements using calibrated foils of variable thickness are consistent with theory. Measurements of the X-ray dose as a function of the delay between the laser and electron beams show a 24-ps full width at half maximum (FWHM) window, as predicted by theory, in contrast with a measured timing jitter of 1.2 ps, which contributes to the stability of the source. In addition, K-edge radiographs of a Ta foil obtained at different electron beam energies clearly demonstrate the γ^2-tunability of the source and show very good agreement with the theoretical divergence-angle dependence of the X-ray spectrum. Finally, electron bunch shortening experiments using velocity compression have also been performed and durations as short as 300 fs rms have been observed using coherent transition radiation; the corresponding inferred peak X-ray flux approaches 10^{19} photons/s.

Keywords: Calibrated foils; Compton scattering; Relativistic electron beam; Velocity compression; X-ray source

1. INTRODUCTION

Remarkable advances in ultrashort pulse laser technology based on chirped-pulse amplification (CPA; Perry & Mourou, 1994; Barty *et al.*, 1996; Mourou *et al.*, 1998; Umstadter *et al.*, 1998), and the recent development of high-brightness, relativistic electron sources (Biedron *et al.*, 1999; Lawson *et al.*, 1999; Yu *et al.*, 1999) allow the design of novel, compact, monochromatic, tunable, femtosecond X-ray sources using Compton scattering (Esarey *et al.*, 1993, 1995; Greiner & Reinhardt, 1994; Ride *et al.*, 1995; Bula *et al.*, 1996; Hartemann & Kerman, 1996; Hartemann *et al.*, 1996; Leemans *et al.*, 1996, 1997; Schoenlein *et al.*, 1996; Burke *et al.*, 1997; Litvinenko *et al.*, 1997; Hartemann, 1998; Bamber *et al.*, 1999). Such new light sources are expected to have a major impact in a number of important fields of research, including the study of fast structural dynamics (Robb, 1995; Chin *et al.*, 1999; Rose-Petruck *et al.*, 1999; Siders *et al.*, 1999; Lindenberg *et al.*, 2000), advanced biomedical imag-

Address correspondence and reprint requests to: F.V. Hartemann, Lawrence Livermore National Laboratory, L-280, P.O. Box 808, Livermore, CA 94551-0808, USA. E-mail: hartemann1@llnl.gov

ing (Fitzgerald, 2000), and advanced time-resolved radiography of high-Z materials. In particular, the unique conditions of atomic-scale interactions have led to a recent experimental push to develop high-brightness, femtosecond, hard X-ray sources. The energy levels relevant to the inner-shell electron properties, which are responsible for most fundamental atomic-scale effects, require photon energies well above those generated by modern ultrafast laser systems, which can only probe the outermost electron levels. Furthermore, the short time scales associated with atomic motion, tens to hundreds of femtoseconds, require much shorter pulses than those provided by synchrotron-based X-ray sources. Finally, high brightness is required to allow for single-shot diffraction or radiography experiments and to yield images at a discrete moment in time to study the progression of dynamic events. The development of a system capable of making measurements on these scales would open up regions of currently underexplored science, such as phase transitions in materials under shock loading and chemical reaction dynamics.

In corollary, a growing number of research groups worldwide are exploring different X-ray production mechanisms such as ultrafast, laser-driven K_α sources (Gu *et al.*, 2001), X-ray free-electron lasers (FELs; Arthur *et al.*, 1995), electron bunch slicing in synchrotrons (Zholents & Zolotorev, 1996; Schoenlein *et al.*, 2000), and Compton scattering (Schoenlein *et al.*, 1996). Although experimental measurements have been demonstrated using some of these techniques (Chin *et al.*, 1999; Siders *et al.*, 1999; Cavalleri *et al.*, 2000), the relative paucity of such high-brightness, ultrafast sources has limited their widespread application. There are also large regions of the energy spectrum where no bright source has yet been demonstrated. Within this context, the Picosecond Laser-Electron Inter-Action for the Dynamic Evaluation of Structures (PLEIADES) project was designed to provide ultrashort (300 fs–3 ps), tunable (10–100 keV) X-ray pulses at a peak brightness of up to 10^{18} photons/(mm^2 × mrad^2 × s × 0.1% bandwidth), to perform single-shot diffraction and radiography experiments in high-Z materials. To meet these exacting design goals, with a special emphasis on the important requirements of tunability and high photon energies, Compton scattering was chosen as the most promising technique. A series of unique challenges arose from that approach, including the production and transport of high-brightness electron bunches that are synchronized with terawatt laser pulses to within a picosecond; pointing and centering accuracies in the 100 μrad and 10 μm ranges for both beams; and the implementation of an adequate suite of laser, electron beam, and X-ray diagnostics, such as frequency-resolved optical gating (FROG), optical transition radiation (OTR), coherent transition radiation (CTR), energy spectrometry, quadrupole scans, streak camera measurements, and X-ray CCD measurements.

This article is organized as follows: The theory of Compton scattering is first briefly reviewed; an overview of the PLEIADES major subsystems is then given, followed by a description of the experimentally measured X-ray characteristics and a comparison with theory; finally, an outline of upcoming upgrades and experiments is presented in the conclusion, together with a few new ideas aimed at further improving the brightness of future Compton scattering X-ray sources.

2. COMPTON SCATTERING THEORY

This section is intended as an overview of some of the salient features of Compton scattering, in the linear regime; for more information, the reader should consult Hartemann *et al.* (2001) and Hartemann (2002). The linear regime corresponds to small laser radiation pressures, where the normalized vector potential satisfies the condition

$$A_0 = \frac{e\sqrt{A_\mu A^\mu}}{m_0 c} \ll 1. \tag{1}$$

In this situation, the electron motion in its original rest frame is a simple transverse oscillation at the Doppler-shifted laser frequency, and it radiates as a dipole. In Eq. (1), $A_\mu = (\varphi, \mathbf{A})$ is the 4-potential of the laser wave, e is the charge of the electron, m_0 its rest mass, and c is the speed of light. As the electric field can be expressed as

$$\mathbf{E} = -\nabla\varphi - \partial_t \mathbf{A}, \tag{2}$$

it is easily seen that for a monochromatic wave of pulsation ω_0, and in the Coulomb gauge, we have

$$A_0 = \frac{eE_0}{\omega_0 m_0 c}, \tag{3}$$

where E_0 is the characteristic strength of the laser electric field.

The physical interpretation of the normalized vector potential is straightforward: On the one hand, considering a monochromatic plane wave of wavelength λ_0, the energy density is

$$\frac{dW}{d\nu} = \varepsilon_0 \frac{E^2}{2} + \frac{B^2}{2\mu_0} = \varepsilon_0 E^2 = \varepsilon_0 E_0^2 \langle \sin^2(\omega_0 t)\rangle = \frac{1}{2}\varepsilon_0 E_0^2; \tag{4}$$

on the other hand, this quantity can be interpreted in terms of photon density, and we have

$$\frac{dW}{d\nu} = n_\gamma \hbar\omega_0 = \frac{1}{2}\varepsilon_0 E_0^2. \tag{5}$$

Here, ε_0 is the permittivity of vacuum. Using the definition of the normalized vector potential, we find that

$$n_\gamma = A_0^2 \frac{1}{2}\varepsilon_0 \left(\frac{\omega_0 m_0 c}{e}\right)^2 \frac{1}{\hbar\omega_0} = \left(\frac{A_0}{2}\right)^2 \frac{1}{\lambda_0 \lambda\!\!\!^{-}_C r_0}, \tag{6}$$

https://doi.org/10.1017/S0263034604223059 Published online by Cambridge University Press

where we have introduced the electron reduced Compton wavelength, $\lambda\!\!\!^{-}_C = \hbar/m_0c$, and the classical electron radius, $r_0 = e^2/4\pi\varepsilon_0 m_0 c^2 = \alpha\lambda\!\!\!^{-}_C$; here, α is the fine structure constant. Thus, a simple and elegant result is obtained: The normalized vector potential is directly related to the number of photons contained in a cube with a side that is the geometrical mean of the classical and quantum electrodynamic scale lengths, and the radiation wavelength.

In the specific case of a linearly polarized Gaussian laser pulse, the electric field at the focal plane takes the form

$$\mathbf{E}(r, z = 0, t) = \hat{\mathbf{x}} E_0 \exp\left[-\left(\frac{t}{\Delta t}\right)^2 - \left(\frac{r}{w_0}\right)^2\right]\sin(\omega_0 t), \quad (7)$$

and we can use the Poynting vector $\mathbf{S} = \mathbf{E} \times \mathbf{H}$, to evaluate the normalized vector potential: We first have

$$\begin{aligned}\mathbf{S} &= \mathbf{E} \times \frac{\mathbf{B}}{\mu_0} = \frac{1}{\mu_0 c}\mathbf{E} \times \mathbf{E} = \frac{\hat{\mathbf{z}}}{\mu_0 c} E^2 \\ &= \hat{\mathbf{z}}\,\frac{E_0^2}{\mu_0 c}\exp\left(-2\,\frac{t^2}{\Delta t^2} - 2\,\frac{r^2}{w_0^2}\right)\sin^2(\omega_0 t) \\ &= \hat{\mathbf{z}}\,\frac{d^2W}{2\pi r dr dt}. \end{aligned} \quad (8)$$

Equation (8) can easily be integrated to yield the total energy in the laser pulse:

$$\begin{aligned}W_0 &= \int_0^\infty 2\pi r dr \int_{-\infty}^{\infty} \frac{E_0^2}{\mu_0 c}\exp\left(-2\,\frac{t^2}{\Delta t^2} - 2\,\frac{r^2}{w_0^2}\right)\sin^2(\omega_0 t) dt \\ &= \frac{E_0^2}{\mu_0 c}\,\frac{1}{2}\left(\sqrt{\frac{\pi}{2}}\right)^3 w_0^2 \Delta t. \end{aligned} \quad (9)$$

Using Eq. (9) and the relation between the normalized potential and the electric field, we have

$$A_0 = \frac{e}{\omega_0 m_0 c}\sqrt{\frac{2\mu_0 c W_0}{\left(\sqrt{\frac{\pi}{2}}\right)^3 w_0^2 \Delta t}}. \quad (10)$$

Here, w_0 is the $1/e^2$ radius of the laser focal spot, and the intensity at full width at half maximum (FWHM) of the laser pulse is equal to $\Delta t\sqrt{2\ln(2)}$; for visible wavelengths, A_0 approaches unity for peak intensities near 10^{17} W/cm^2.

To derive the well-known Compton formula yielding the energy of the Doppler-upshifted photons, the correlation between the initial photon state and the scattered photon 4-wavenumber can be used by considering the conservation of energy and momentum: We have

$$m_0 c u_\mu^0 + \hbar k_\mu^0 = m_0 c u_\mu^s + \hbar k_\mu^s, \quad (11)$$

which can also be expressed as

$$u_\mu^0 + \lambda\!\!\!^{-}_C k_\mu^0 = u_\mu^s + \lambda\!\!\!^{-}_C k_\mu^s, \quad (12)$$

after introducing the Compton wavelength, $\lambda\!\!\!^{-}_C$. In the above, $u_\mu = (\gamma, \gamma\boldsymbol{\beta}) = dx_\mu/d\tau$ is the normalized 4-velocity, and $k_\mu = (\omega c^{-1}, \mathbf{k})$ is the 4-wavenumber. In addition, the 4-velocity is normalized, with $u_\mu u^\mu = -1$, and the photon mass shell condition, or dispersion relation, implies that $k_\mu k^\mu = 0$. Using the first condition, we have

$$u_\mu^s = u_\mu^0 + \lambda\!\!\!^{-}_C k_\mu^0 - \lambda\!\!\!^{-}_C k_\mu^s, \qquad u_\mu^s u_s^\mu = -1, \quad (13)$$

which yields

$$[u_\mu^0 + \lambda\!\!\!^{-}_C(k_\mu^0 - k_\mu^s)][u_0^\mu + \lambda\!\!\!^{-}_C(k_0^\mu - k_s^\mu)] + 1 = 0. \quad (14)$$

Explicitly developing Eq. (14), we first find that

$$u_\mu^0 u_0^\mu + 2\lambda\!\!\!^{-}_C u_\mu^0(k_0^\mu - k_s^\mu) + \lambda\!\!\!^{-2}_C(k_\mu^0 - k_\mu^s)(k_0^\mu - k_s^\mu) + 1 = 0; \quad (15)$$

using the normalization of the 4-velocity, this reduces to

$$2\lambda\!\!\!^{-}_c u_\mu^0(k_0^\mu - k_s^\mu) + \lambda\!\!\!^{-2}_c(k_\mu^0 k_0^\mu - 2k_\mu^s k_0^\mu + k_\mu^s k_s^\mu) = 0; \quad (16)$$

finally, the dispersion relation allows us to eliminate the quadratic terms in $k_\mu k^\mu$, to obtain the sought-after relation between the initial and final photon states:

$$k_\mu^s(u_0^\mu + \lambda\!\!\!^{-}_C k_0^\mu) = k_\mu^0 u_0^\mu. \quad (17)$$

In vector form, this result can be expressed as

$$k_s = \frac{\gamma_0 k_0 - \mathbf{u}_0 \cdot \mathbf{k}_0}{(\gamma_0 + \lambda\!\!\!^{-}_C k_0) - \hat{n}\cdot(\mathbf{u}_0 + \lambda\!\!\!^{-}_C \mathbf{k}_0)}. \quad (18)$$

In the case where recoil is negligible, we have $\lambda\!\!\!^{-}_C k_\mu^0/u_\mu^0 \ll 1$, and we recover the well-known Thomson scattering result:

$$\frac{k_s}{k_0} = \frac{\gamma_0 - \hat{n}_0 \cdot \mathbf{u}_0}{\gamma_0 - \hat{n}\cdot\mathbf{u}_0}. \quad (19)$$

We can define the incidence angle, φ, and the scattering angle, θ, to recast Eq. (19) as

$$\frac{k_s}{k_0} = \frac{\gamma_0 - u_0\cos\varphi}{\gamma_0 - u_0\cos\theta} = \frac{1 - \beta_0\cos\varphi}{1 - \beta_0\cos\theta}. \quad (20)$$

The differential scattering cross section can be derived by starting in the rest frame of the electron and boosting back to laboratory frame; the main steps of the derivations are outlined here. In the Thomson scattering limit, the incident photon has a very small energy compared to the electron rest mass; hence, the scattered photon has the same energy as the incident photon in the electron rest frame. For the case of an electron distribution at rest, the total number of scattered photons per unit time is simply the overlap integral of the

https://doi.org/10.1017/S0263034604223059 Published online by Cambridge University Press

product of the total Thomson cross section multiplied by the flux of incident photons, leading to

$$N_s' = \int c\sigma n_e'(\mathbf{r},t) n_\gamma'(\mathbf{r},t) d^3\mathbf{r}dt, \tag{21}$$

where σ is the total Compton scattering cross section, and $n_\gamma'(\mathbf{r},t)$ and $n_e'(\mathbf{r},t)$ are, respectively, the photon and electron density in the electron beam rest frame. To generalize this for a relativistic electron beam, we note that that the total number of scattered photons is invariant under a Lorentz transformation, and that the above expression can be expressed in covariant form as the integration of the product of the electron 4-current density, $j_\mu = n_e e c u_\mu$, and the photon 4-flux, $\phi_\mu = c n_\gamma k_\mu$, which yields

$$N_s = \frac{\sigma}{ce}\int j^\mu \phi_\mu d^4x = \sigma c \int \left(1 - \boldsymbol{\beta}_e\cdot\mathbf{k}\,\frac{c}{\omega}\right) n_e(\mathbf{r},t) n_\gamma(\mathbf{r},t) d^3\mathbf{r}dt. \tag{22}$$

In the case of a single electron, the density is a delta-function: $n_e(\mathbf{r},t) = \delta[\mathbf{r} - \mathbf{r}_e(t)]$, where $\mathbf{r}_e(t)$ describes the electron trajectory. Thus, the rate of scattered photons by a single electron becomes

$$\frac{dN_s}{dt} = \sigma c\left(1 - \boldsymbol{\beta}_e\cdot\mathbf{k}\,\frac{c}{\omega}\right) n_\gamma[\mathbf{r}_e(t),t]. \tag{23}$$

Likewise, the rate of photons scattered into a given solid angle is given by

$$\frac{dN_s}{d\Omega dt} = c\left(1 - \boldsymbol{\beta}_e\cdot\mathbf{k}\,\frac{c}{\omega}\right) n_\gamma(\mathbf{r}_e,t)\,\frac{d\sigma}{d\Omega}, \tag{24}$$

while the rate scattered per unit frequency is given by

$$\begin{aligned}\frac{dN_s}{d\omega_s d\Omega dt} &= c\left(1 - \boldsymbol{\beta}_e\cdot\mathbf{k}\,\frac{c}{\omega}\right) n_\gamma \frac{d\sigma}{d\Omega d\omega_s} \\ &= c\left(1 - \boldsymbol{\beta}_e\cdot\mathbf{k}\,\frac{c}{\omega}\right) n_\gamma(\mathbf{r}_e,t)\,\frac{d\sigma}{d\Omega}\,\delta[\omega_s - \omega\mathcal{D}(\phi,\theta)],\end{aligned} \tag{25}$$

where $d\sigma/d\Omega$ is the differential scattering cross section, ω_s is angular frequency of the scattered photon, and $\mathcal{D}(\phi,\theta)$ is the relativistic Doppler upshift of the scattered photon, defined in Eq. (19), which depends on the angle of incidence, ϕ, and the scattering angles, θ, between the observation direction and the electron direction. Equation (25) completely describes the temporal, spectral, and spatial properties of the scattered X-ray distribution.

A general, covariant expression for the differential cross section in Eq. (25) can be derived by first transforming the wave vector of incident photon into the electron rest frame. The corresponding rest frame differential cross section can then be transformed back into the laboratory frame. If we represent the incident laser polarization vector in the electron rest frame as $\boldsymbol{\alpha}'$, the differential cross section is given by the simple expression

$$\frac{d\sigma}{d\Omega'} = r_0^2 |\boldsymbol{\eta}'\cdot\boldsymbol{\alpha}'|^2, \tag{26}$$

where $\boldsymbol{\eta}'$ is the scattered photon polarization, and r_0 is the classical electron radius.

Using the angular notation defined in Figure 1, and summing over final polarization states yields the Compton scattering cross section, as expressed in the initial rest frame of the electron, for an arbitrary linearly polarized incident photon:

$$\begin{aligned}\frac{1}{r_0^2}\frac{d\sigma}{d\Omega'} &= \alpha_x'^2(1 - \cos^2\phi_e'\sin^2\theta_e') + \alpha_y'^2(1 - \sin^2\phi_e'\sin^2\theta_e') \\ &\quad + \alpha_z'^2(1 - \cos^2\theta_e') \\ &\quad - 2\alpha_x'\alpha_y'(\cos\phi_e'\sin\theta_e')(\sin\phi_e'\sin\theta_e') \\ &\quad - 2\alpha_x'\alpha_z'\cos\theta_e'(\cos\phi_e'\sin\theta_e'). \\ &\quad - 2\alpha_x'\alpha_z'\cos\theta_e'(\sin\phi_e'\sin\theta_e').\end{aligned} \tag{27}$$

To make Eq. (27) practical, it is desirable to express the components of the rest frame incident laser polarization vector in terms of laboratory frame coordinates. In addition, to facilitate the inclusion of three-dimensional (3D) effects resulting from the focusing of the electron and laser beams, the direction of the individual electrons and photon wave vectors in the each beam are assumed to deviate slightly from the average directions defined above. As shown in Figure 2 (top), the direction of each incident photon wave vector will be specified by an additional rotation ξ_x about the y-axis, and a rotation ξ_y about the x-axis. Likewise, an electron laboratory frame, with Cartesian coordinates (x_e, y_e, z_e) is defined such that the z_e-axis is collinear with the individual electron direction; this frame is specified by a rotation ξ_{xe} about the y_e-axis and an angle ξ_{ye} about the x_e-axis, as shown in Figure 2 (bottom).

To simplify the Lorentz transformations to and from the electron rest frame, our approach is to first calculate the cross section in a laboratory frame aligned with the electron velocity, then rotate back to the laboratory frame, which is generally chosen so that the laser focus is the origin, while the direction of propagation of the laser pulse and its polarization, in the linear case, can be used to define its axes. To Lorentz transform the components of the polarization vector, we use the transform of the electromagnetic field tensor:

$$F_{\mu\nu}' = \frac{\partial x_\mu'}{\partial x_\lambda}\frac{\partial x_\nu'}{\partial x_\sigma}F_{\lambda\sigma}; \tag{28}$$

https://doi.org/10.1017/S0263034604223059 Published online by Cambridge University Press

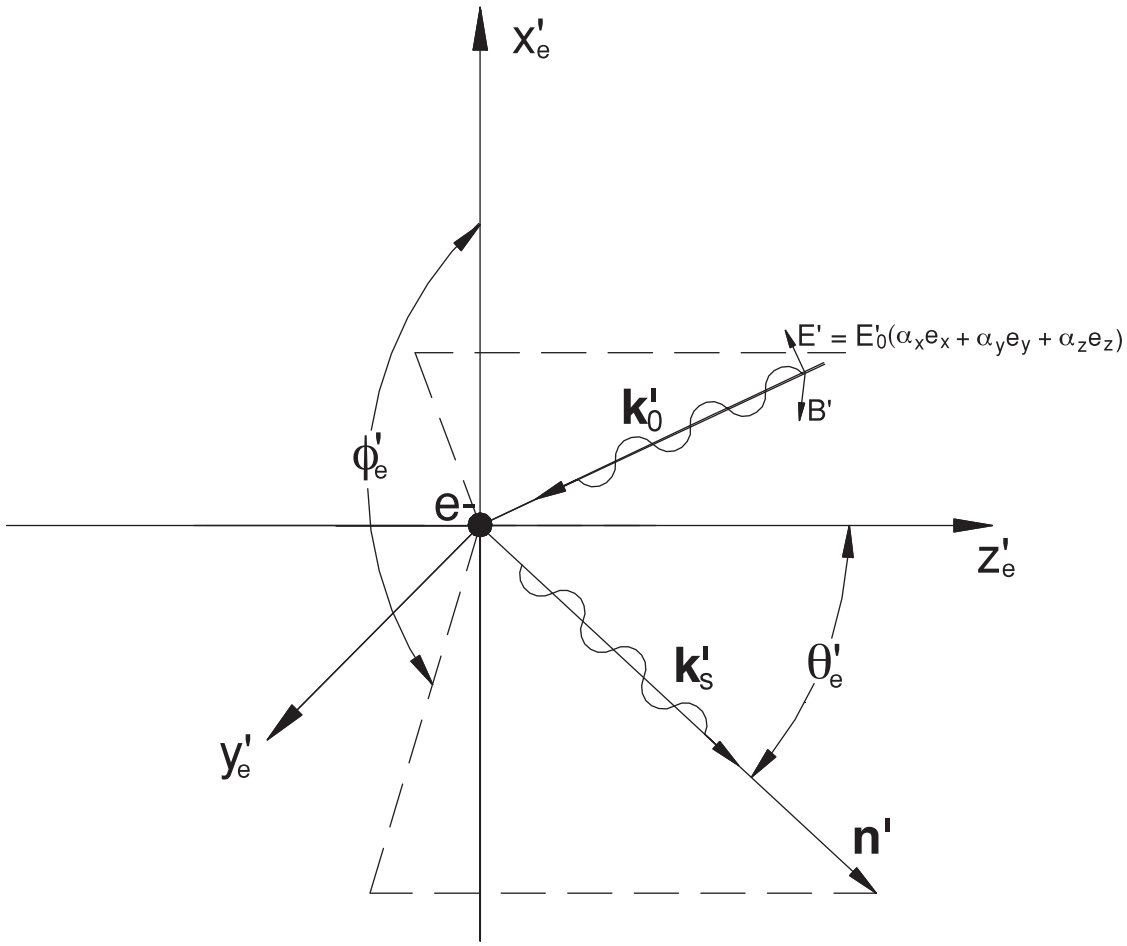

Fig. 1. Compton scattering interaction geometry in the electron rest frame.

we then extract the polarization vector by noting that, in general, $\boldsymbol{\alpha} = \mathbf{E}/|\mathbf{E}|$. After lengthy algebra, we obtain:

$$\alpha'_{xe} = \frac{1}{\mathcal{D}'}\left\{\begin{array}{l}\cos\phi_p(\cos(\phi_x - \xi_{xe})(1 + \beta\sin\xi_y\sin\xi_{ye}) \\ +\beta\cos\xi_y\cos\xi_{ye}) - \sin\phi_p\sin(\theta_x - \xi_{xe}) \\ \times(\sin\xi_y + \beta\sin\xi_{ye})\end{array}\right\},$$

$$\alpha'_{ye} = \frac{1}{\mathcal{D}'}\left\{\begin{array}{l}\cos\phi_p\sin(\theta_x - \xi_{xe})(\sin\xi_{ye} + \beta\sin\xi_y) \\ +\sin\phi_p[\cos(\theta_x - \xi_{xe})(\beta + \sin\xi_y\sin\xi_{ye}) \\ +\cos\xi_y\cos\xi_{ye}]\end{array}\right\},$$

$$\alpha'_{ze} = \frac{-1}{\gamma\mathcal{D}'}\left\{\begin{array}{l}\cos\phi_p\sin(\theta_x - \xi_{xe})\cos\xi_{ye} \\ +\sin\phi_p(\sin\xi_y\cos\xi_{ye}\sin(\theta_x - \xi_{xe}) \\ -\cos\xi_y\sin\xi_{ye})\end{array}\right\};$$

$$\mathcal{D}' = \frac{\omega'_0}{\omega_0} = \gamma\left(1 - \beta\cdot c\,\frac{\mathbf{k}_0}{\omega_0}\right),$$

$$\theta_x = \theta_0 + \xi_x. \tag{29}$$

Equation (29) expresses the normalized components of the polarization vector in the electron beam rest frame in terms of the laser and electron direction, the electron beam energy, and the laser polarization. Note that in the plane wave approximation, where $\xi_x = \xi_y = 0$, Eq. (29) reduces to

$$\alpha'_{xe} \approx \frac{1}{\mathcal{D}'}\left\{\begin{array}{l}\cos\phi_p[\cos(\theta_0 - \xi_{xe}) + \beta\cos\xi_{ye}] \\ -\beta\sin\phi_p\sin\xi_{ye}\sin(\theta_0 - \xi_{xe})\end{array}\right\},$$

$$\alpha'_{ye} \approx \frac{1}{\mathcal{D}'}\left\{\begin{array}{l}\cos\phi_p\sin(\theta_0 - \xi_{xe})\sin\xi_{ye} \\ +\sin\phi_p[\beta\cos(\theta_0 - \xi_{xe}) + \cos\xi_{ye}]\end{array}\right\},$$

$$\alpha'_{ze} \approx \frac{-1}{\gamma\mathcal{D}'}\left[\begin{array}{l}\cos\phi_p\sin(\theta_0 - \xi_{xe})\cos\xi_{ye} \\ +\sin\phi_p\sin\xi_{ye}\end{array}\right]. \tag{30}$$

Equation (29) can now be transformed to the electron laboratory frame described above by considering the Lorentz transform of the 4-wavenumber, k_μ. Within this frame, the scattered photon direction is defined by the wave-vector

https://doi.org/10.1017/S0263034604223059 Published online by Cambridge University Press

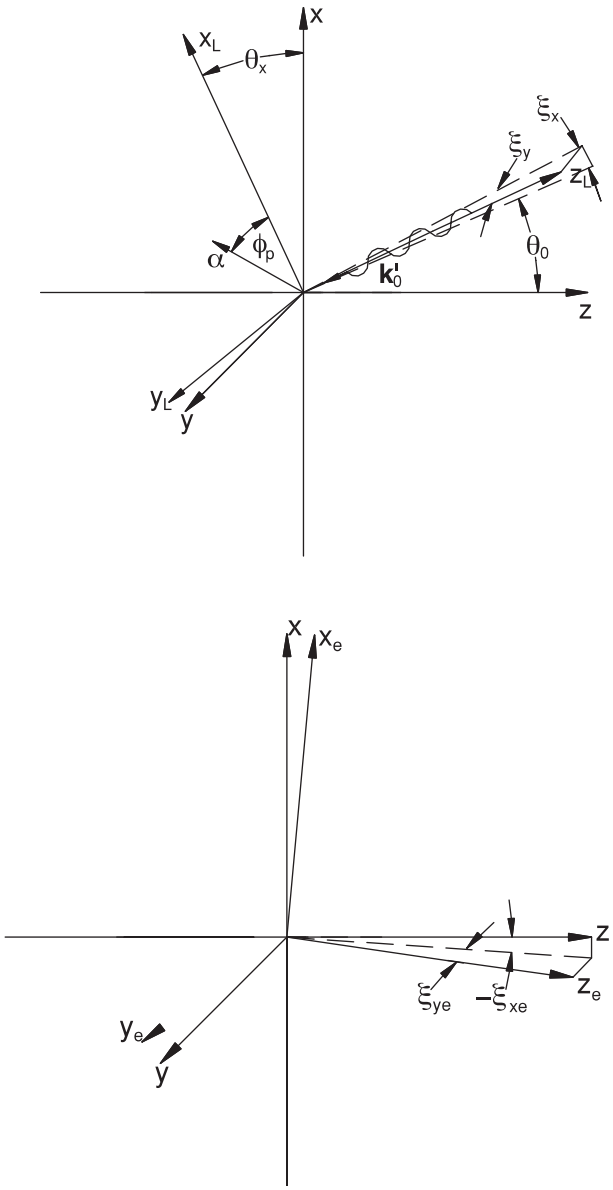

Fig. 2. Top: Illustration of the laser incident direction and polarization. $\boldsymbol{\alpha}$ is the direction of the polarization vector of the laser, where ϕ_p represents the rotation angle of $\boldsymbol{\alpha}$ about the z_L-axis. Bottom: Illustration of the electron incident direction. The electron beam is incident along the z-axis, but the direction of each electron deviated by the angles specified by ξ_{xe} and ξ_{ye}.

$$\mathbf{k}'_s = \frac{\omega'_s}{c}\left(\sin\theta'_e\cos\phi'_e\hat{x}'_e + \sin\theta'_e\sin\phi'_e\hat{y}'_e + \cos\theta'_e\hat{z}'_e\right), \tag{31}$$

where θ'_e and ϕ'_e specify the scattered photon direction about the positive z-axis in the rest frame, as shown in Figure 1. Because we are primarily interested in the Thomson scattering limit, the scattered photon frequency, ω'_s, is taken to be equal to the incident frequency ω'_0. The scattered photon energy in the rest frame, ω'_s, is expressed in terms of the photon energy in the lab frame, ω_s, by using the Lorentz transformation once again, from the laboratory frame to the rest frame:

$$\frac{\omega'_s}{c} = \gamma\left(\frac{\omega_s}{c} - \boldsymbol{\beta}\cdot\mathbf{k}_s\right) = \frac{\omega_s}{c}\gamma[1-\beta\cos(\theta_e)], \tag{32}$$

where θ_e is the angle of the scattered photon with respect to the z_e-axis in the electron laboratory frame. Applying the Thomson scattering limit approximation and using Eq. (32) leads to

$$\begin{aligned}\frac{\omega_s}{\omega_0} &= \frac{\mathcal{D}'(\theta_x,\xi_y,\xi_{xe},\xi_{ye})}{1-\beta\cos(\theta_e)} \equiv \mathcal{D}(\theta_x,\xi_y,\xi_{xe},\xi_{ye},\theta_e)\\ &\approx \frac{2\gamma\mathcal{D}'(\theta_x,\xi_y,\xi_{xe},\xi_{ye})}{1+\gamma^2\theta_e^2}.\end{aligned} \tag{33}$$

For a head-on collision, we recover the well-known photon maximum Doppler upshift of approximately $4\gamma^2$, whereas for a 90° collision, the upshift approaches $2\gamma^2$. Furthermore, the variation of the scattered photon energy as a function of the observation angle, θ_e, can be approximated by a Lorentzian with a FWHM equal to $1/\gamma$.

Finally, the propagation direction of the scattered photon, as measured in the rest frame, can be expressed in terms of laboratory angles by transforming $\mathbf{k}_s$ back. In addition, we will use the fact that

$$\frac{d\sigma}{d\Omega} = \frac{d\sigma}{d\Omega'}\frac{d\Omega'}{d\Omega} = \frac{d\sigma}{d\Omega'}\frac{d(\cos\theta'_e)}{d\cos\theta_e} = \frac{d\sigma}{d\Omega'}\left\{\frac{1-\beta^2}{[1-\beta\cos(\theta_e)]^2}\right\}, \tag{34}$$

where, $d\Omega = \sin(\theta)d\theta d\phi = -d\cos(\theta)d\phi$, and where we have used the fact that for the case under consideration, $d\phi = d\phi'$. This leads to the sought-after expression for the differential cross section in the laboratory frame:

$$\begin{aligned}\frac{d\sigma}{d\Omega}(\theta_e,\phi_e)\frac{[1-\beta\cos(\theta_e)]^2}{r_0^2(1-\beta^2)} &= \alpha'^2_x\left\{1-\frac{\cos^2(\phi_e)\sin^2(\theta_e)}{\gamma^2[1-\beta\cos(\theta_e)]^2}\right\}\\ &+ \alpha'^2_y\left\{1-\frac{\sin^2(\phi_e)\sin^2(\theta_e)}{\gamma^2[1-\beta\cos(\theta_e)]^2}\right\}\\ &+ \alpha'^2_z\left\{1-\left[\frac{\cos(\theta_e)-\beta}{1-\beta\cos(\theta_e)}\right]^2\right\}\\ &- 2\alpha'_x\alpha'_y\frac{\cos(\phi_e)\sin(\phi_e)\sin^2(\theta_e)}{\gamma^2[1-\beta\cos(\theta_e)]^2}\\ &-2\alpha'_x\alpha'_z\frac{[\cos(\theta_e)-\beta]\cos(\phi_e)\sin(\theta_e)}{\gamma[1-\beta\cos(\theta_e)]^2}\\ &-2\alpha'_y\alpha'_z\frac{[\cos(\theta_e)-\beta]\sin(\phi_e)\sin(\theta_e)}{\gamma[1-\beta\cos(\theta_e)]^2}.\end{aligned} \tag{35}$$

At this point, a three-dimensional time and frequency-domain model of the scattering process can be developed by

https://doi.org/10.1017/S0263034604223059 Published online by Cambridge University Press

considering the phase-space photon density of the focusing laser pulse, which can be derived using Fourier analysis and the paraxial wave approximation (Hartemann *et al.*, 1998, 2001; Hartemann, 2002). The laser frequency spectrum provides the incident photon energy distribution, whereas the transverse momentum distribution is obtained by rescaling the transverse wave number spectrum of the focusing wave by a factor $\hbar$. The three-dimensional spatial photon density is proportional to the intensity of the laser pulse, given by

$$n_\gamma(r,z,t) \propto I(r,z,t) = \frac{I_0}{1+\left(\frac{z}{z_0}\right)^2} \exp\left\{-2\left(\frac{t}{\Delta t}\right)^2 - 2\left[\frac{r}{w_0\sqrt{1+\left(\frac{z}{z_0}\right)^2}}\right]^2\right\} \times \langle \sin^2(\omega_0 t)\rangle, \quad (36)$$

for a cylindrical focus and a linearly polarized wave; $\langle \sin^2(\omega_0 t)\rangle = 1/2$. Finally, for a Fourier-transform limited pulse, which corresponds to the minimum uncertainty according to the Heisenberg Principle, the photon phase space conjugate coordinates are uncorrelated.

Most of the theoretical results and analyses presented in this article result from a three-dimensional time and frequency-domain code based on the formalism described above, and from a three-dimensional frequency-domain code described in Hartemann *et al.* (2001), which uses the Hartemann–Le Foll (HLF) Theorem.

The HLF Theorem will be used here to describe some of the important features of Compton scattering in the case of an electron beam with energy spread and emittance.

The HLF Theorem states that in the linear regime, where the 4-potential amplitude satisfies the condition $eA/m_0c \ll 1$, and in the absence of radiative corrections (Dirac, 1938; Hartemann & Kerman, 1996; Hartemann, 1998), where the frequency cutoff is $\omega \ll m_0c^2/\hbar$, as measured in the electron frame, the spectral photon number density scattered by an electron interacting with an arbitrary electromagnetic field distribution in vacuum is given by the momentum space distribution of the incident vector potential at the Doppler-shifted frequency:

$$\frac{d^2N_x(k_\mu^s)}{d\omega_s d\Omega} = \frac{\alpha}{(2\pi)^4}\frac{1}{\gamma_0^2\omega_s}\left|\boldsymbol{k}_s \times \int_{\mathbb{R}^3}\left[1+\left(\frac{\boldsymbol{k}}{\kappa_s}\right)\boldsymbol{u}_0\cdot\right] \times \tilde{\boldsymbol{A}}\left[\omega_s - \frac{\boldsymbol{u}_0}{\gamma_0}\cdot(\boldsymbol{k}_s-\boldsymbol{k}),\boldsymbol{k}\right]\exp(i\boldsymbol{k}\cdot\boldsymbol{k}_0)d^3\boldsymbol{k}\right|^2. \quad (37)$$

Here, $k_\mu^s = (\omega_s, \boldsymbol{k}_s) = \omega_s(1,\hat{\mathbf{n}})$ is the 4-wavenumber of the wave scattered in the observation direction $\hat{\mathbf{n}}$, at the frequency ω_s; $\alpha = e^2/2\varepsilon_0 hc \simeq 1/137.036$ is the fine structure constant; $u_\mu^0 = (\gamma_0, \boldsymbol{u}_0)$ is the electron initial 4-velocity; $x_\mu^0 = (0, \boldsymbol{x}_0)$ is its initial 4-position; and we have introduced the scattered light-cone variable, $\kappa_s = -u_0^\mu k_\mu^s = \gamma_0\omega_s - \boldsymbol{u}_0\cdot\boldsymbol{k}_s$. The term $[1+(\boldsymbol{k}/\kappa_s)\boldsymbol{u}_0\cdot]$ is to be considered as an operator acting on the Fourier transform of the spatial components of the 4-potential, $A_\mu = (\mathrm{V}, \boldsymbol{A})$,

$$\tilde{A}_\mu(k_\nu) = \frac{1}{\sqrt{2\pi^4}}\int_{\mathbb{R}^4} A_\mu(x^\nu)\exp(ik_\nu x^\nu)d^4k_\nu, \quad (38)$$

while the term $\exp(i\boldsymbol{k}\cdot\boldsymbol{x}_0)$ gives rise to the coherence factor (Hogan *et al.*, 1998; Hartemann, 2000).

We now consider the case of a linearly polarized plane wave with an arbitrary temporal profile: The 4-potential is $A_\mu(\phi) = \hat{\mathbf{x}}A_0 g(\phi)e^{-i\phi}$, where $\phi = -k_\mu^0 x^\mu$, and $k_\mu^0 = (1,0,0,1)$, for a wave propagating along the z-axis. Introducing the temporal Fourier transform of the pulse envelope, $\tilde{g}(\omega) = \int_{-\infty}^{+\infty} g(t)e^{-i\omega t}dt/\sqrt{2\pi}$, we have

$$\tilde{A}_\mu(k_\nu) = \hat{\mathbf{x}}\sqrt{2\pi}^3 A_0\delta(k_x)\delta(k_y)\delta(\omega-k_z)\tilde{g}(1-\omega), \quad (39)$$

where $\delta(\omega - k_z)$ corresponds to the pulse propagation, and $\tilde{g}(1-\omega)$ is the spectrum of the pulse, centered around the normalized frequency $\omega_0 = 1$, in our units. Applying the HLF Theorem, we immediately find

$$\frac{d^2N_x}{d\omega_s d\Omega} = \frac{\alpha}{2\pi}\omega_s\frac{A_0^2}{\kappa_0^2}\left|\hat{\mathbf{n}}\times\left(\hat{\mathbf{x}}+\frac{u_{0x}}{\kappa_0}\hat{\mathbf{z}}\right)\right|^2\tilde{g}^2\left(1-\frac{\kappa_0^s}{\kappa_0}\right), \quad (40)$$

where $\kappa_0 = \gamma_0 - \boldsymbol{u}_0\cdot\hat{\mathbf{z}} = \gamma_0 - u_{0z}$, and $\kappa_0^s = \omega_s(\gamma_0 - \boldsymbol{u}_0\cdot\hat{\mathbf{n}})$. Introducing the normalized Doppler-shifted frequency $\chi = \kappa_0^s/\kappa_0 = \omega_s(\gamma_0 - \boldsymbol{u}_0\cdot\hat{\mathbf{n}})/(\gamma_0 - u_{0z})$, and the differential scattering cross section, or radiation pattern, $f = |[\hat{\mathbf{n}}\times(\kappa_0\hat{\mathbf{x}}_0 + u_{0x}\hat{\mathbf{z}})]/\kappa_0^2|^2$, this result can be recast as

$$\frac{d^2N_x}{d\omega_s d\Omega} = \frac{\alpha}{2\pi}A_0^2\omega_s f\tilde{g}^2(1-\chi). \quad (41)$$

2.1. The one-dimensional cold spectral density

In the case of a Gaussian pulse envelope, where $g(t) = e^{-t^2/\Delta t^2}$, and for the interaction geometry shown in Figure 3, Eq. (41) takes the familiar form

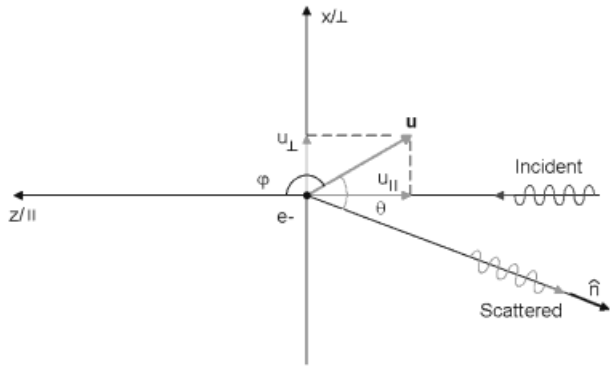

Fig. 3. Schematic of the three-dimensional Compton scattering geometry used for the frequency-domain code.

https://doi.org/10.1017/S0263034604223059 Published online by Cambridge University Press

$$\frac{d^2N_x}{d\omega_s d\Omega} = \frac{\alpha}{4\pi} A_0^2 \Delta\phi^2 \omega_s \exp\left\{-\frac{\Delta\phi^2}{2}\left[\chi(\omega_s,\gamma_0,\theta,\varphi)-1\right]^2\right\} \times \frac{\left[\gamma_0\cos(\theta+\varphi)-u_0\cos\theta\right]^2}{\left[\gamma_0-u_0\cos\varphi\right]^4}. \quad (42)$$

Here, φ is the incidence angle between the initial electron velocity and the direction of propagation of the plane wave, and θ is the scattering angle, measured with respect to the electron initial velocity. Equation (42) clearly shows that the scattering spectral density is proportional to the incident photon number density, as represented by the laser intensity $A_0^2\Delta\phi$, and that the cold spectral bandwidth of the X rays is given by that of the incident laser pulse, $\Delta\phi^{-1} = 1/\omega_0\Delta t$. Equation (42) also indicates that the peak intensity is radiated near the Doppler-shifted frequency, where $\chi(\omega_x,\gamma_0,\theta,\varphi) \simeq 1$; this yields

$$\hbar\omega_x(\gamma_0,\theta,\varphi) \simeq \hbar\omega_0 \frac{\gamma_0-u_0\cos\varphi}{\gamma_0-u_0\cos\theta}.$$

For a head-on collision, where $\varphi = \pi$, the frequency radiated on-axis, for $\theta = 0$, is the same as the well-known free-electron laser (FEL) frequency for an electromagnetic wiggler (Roberson & Sprangle, 1989): For ultrarelativistic (UR) electrons, we recover the well-known relation, $\omega_x = \gamma^2(1+\beta)^2 \simeq 4\gamma^2$.

The angular X-ray energy distribution can be mapped by considering the position of the spectral peak, where $\omega_s = \omega_x$ and $\chi = 1$. We then find that

$$\frac{d^2N_x}{d\omega d\Omega}(\omega_x,\hat{\mathbf{n}}) = \frac{\alpha}{4\pi} A_0^2\Delta\phi^2 \frac{\left[\gamma\cos(\varphi+\theta)-u(\gamma)\cos\theta\right]^2}{\left[\gamma-u(\gamma)\cos\theta\right]\left[\gamma-u(\gamma)\cos\varphi\right]^3}; \quad (43)$$

in the particular case of a head-on collision ($\varphi = \pi$), the angular behavior reduces to

$$\frac{\cos^2\theta}{\left[\gamma-u(\gamma)\cos\theta\right]\left[\gamma+u(\gamma)\right]} \simeq \frac{\gamma-u(\gamma)}{\gamma-u(\gamma)\cos\theta}, \quad (44)$$

where the approximation holds for small angles; the FWHM of the X-ray cone can be derived by further simplifying Eq. (44) for UR electrons and small angles, where we can use the following approximations: $u(\gamma) \simeq \gamma - (1/2\gamma)$, and $\cos\theta \simeq 1 - (\theta^2/2)$, respectively. With this, the angular energy distribution is described by a Lorentzian: $1/[1+(\gamma\theta)^2]$, which has an angular FWHM equal to $2/\gamma$. This well-known behavior of the X-ray frequency-integrated cone (Zholents & Zolotorev, 1996; Schoenlein *et al.*, 2000) is illustrated in Figure 4, where the correlation between the spectral density and the angle is manifest.

Before studying the effect of energy spread and emittance (Carlsten, 1989; Reiser, 1994; Wiedemann, 1999), we also note that the cold, average on-axis brightness of the X-ray source can be estimated by multiplying the spectral brightness by the normalized average electron bunch current $\langle I_b\rangle = q\rho$, where ρ is the repetition rate of the system; by

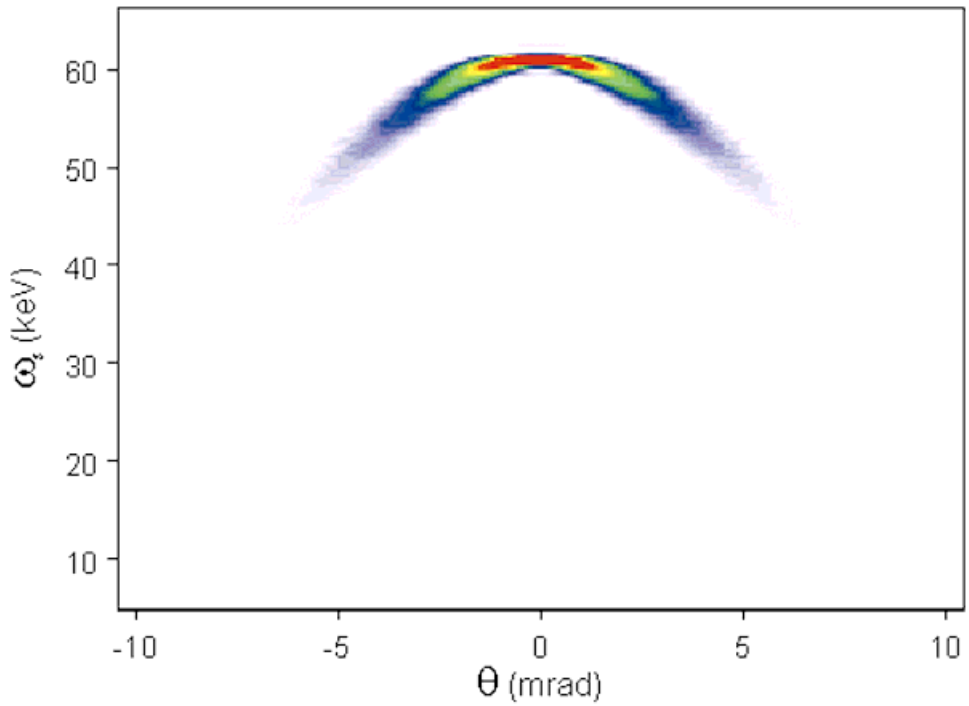

Fig. 4. False color plot of the spectral density of scattered X rays in the *y*–*z* plane resulting from the head-on collision of a 50-MeV electron bunch with $\epsilon_{nx} = 1$ mm·mrad focused to an rms spot size of 20 μm with an 800-nm, 1-ps bandwidth laser pulse polarized in the *x*-direction.

https://doi.org/10.1017/S0263034604223059 Published online by Cambridge University Press

considering a 1 mrad^2 solid angle, $\Delta\Omega = 10^{-6}$, and a 0.1% fractional bandwidth, $\Delta\omega = \omega_x \times 10^{-3}$; and by normalizing the source size to 1 mm^2; with this we obtain

$$\langle B_x \rangle = \frac{\alpha}{4\pi} \frac{\langle I_b \rangle}{\pi r_b^2} A_0^2 \Delta\phi^2 \omega_x \times 10^{-15}, \tag{45}$$

where $\langle B_x \rangle$ is expressed in units of photons/(0.1% bandwidth $\times$ mrad^2 $\times$ mm^2 $\times$ s), and r_b is the electron beam spot size, which we assume to be equal to the laser spot size. The normalized vector potential is given by Eq. (10) as expressed in terms of the laser pulse energy $\mathcal{W}_0$, duration Δt, frequency ω_0, and focal spot size w_0. With this, the main scaling laws for the X-ray brightness, in the case of an electron beam with no emittance, are clearly exhibited: bilinear in the laser pulse energy and electron bunch charge, and inversely proportional to the 4th power of the source size, $1/w_0^2 r_b^2$.

2.2. Energy spread

The formalism used to model the influence of the electron beam phase space topology is now illustrated in the case of a linearly polarized plane wave with an arbitrary temporal profile; in this simple case, analytical results are derived. We introduce the cold, one-dimensional (1D) normalized spectral brightness,

$$\begin{aligned} S_0(\omega,\gamma,\theta,\varphi) &= \frac{4\pi}{\alpha A_0^2 \Delta\phi^2} \frac{d^2 N_x}{d\omega d\Omega} \\ &= \omega \exp\left\{ -\frac{\Delta\phi^2}{2} [\chi(\omega,\gamma,\theta,\varphi) - 1]^2 \right\} f(\gamma,\theta,\varphi). \end{aligned} \tag{46}$$

Note that as S_0 is a function of the electron initial energy, γ, scattering angle, θ, and incident angle, φ, we can perform incoherent summations over the electron initial energy and momentum distributions to study the effects of energy spread and emittance. For conciseness, the scattered frequency is now labeled ω, and the initial electron 4-velocity is labeled as $u_\mu^0 = (\gamma, u)$, were $u = \sqrt{\gamma^2 - 1}$. The use of incoherent summations, although intuitively obvious, can be rigorously justified as shown in Hartemann (2000).

We start with the beam energy spread; the "warm" beam brightness is given by

$$\begin{aligned} &S_\gamma(\omega,\gamma_0,\Delta\gamma,\theta,\varphi) \\ &\quad \simeq \frac{1}{\sqrt{\pi}\Delta\gamma} \int_1^\infty S_0(\omega,\gamma,\theta,\varphi) \exp\left[-\left(\frac{\gamma-\gamma_0}{\Delta\gamma} \right)^2 \right] d\gamma, \\ &\quad \simeq \frac{\omega f(\gamma_0,\theta,\varphi) \exp\left(\dfrac{\mathrm{u}^2}{\mathrm{v}} - \mathrm{w} \right)}{\sqrt{1 + \dfrac{1}{2}\left(\Delta\phi \dfrac{\Delta\gamma}{\gamma_0} \right)^2 \left[\dfrac{\omega}{\gamma_0^2} \dfrac{\cos\varphi - \cos\theta}{(1-\cos\varphi)^2} \right]^2}}, \end{aligned} \tag{47}$$

where we have used a Gaussian distribution to model the beam longitudinal phase space. Note that as

$$\lim_{\Delta\gamma\to 0} \frac{1}{\sqrt{\pi}\Delta\gamma} \exp\left[-\left(\frac{\gamma-\gamma_0}{\Delta\gamma} \right)^2 \right] = \delta(\gamma - \gamma_0),$$

the cold brightness is automatically recovered for a monoenergetic electron beam.

The analytical result in Eq. (47) is obtained by Taylor expanding to second order around the central electron energy, γ_0. The normalization constant is given by

$$\int_1^\infty \exp\left[-\left(\frac{\gamma-\gamma_0}{\Delta\gamma} \right)^2 \right] d\gamma \simeq \sqrt{\pi}\Delta\gamma, \tag{48}$$

an excellent approximation for $\gamma_0 \gg 1$ and $\Delta\gamma/\gamma_0 \ll 1$. Here, $\Delta\gamma$ refers to the energy spread; in addition,

$$a = \frac{\omega}{\gamma_0^3} \frac{(\cos\varphi - \cos\theta)}{(1-\cos\varphi)^2}, \qquad b = \chi(\omega,\gamma_0,\theta,\varphi) - 1,$$

$$\mathrm{u} = \frac{1}{\Delta\gamma^2} \left[1 + \frac{\mathrm{a}}{2} (\Delta\phi\Delta\gamma)^2 \right],$$

$$\mathrm{v} = \frac{\Delta\phi^2}{2} \mathrm{ab}, \quad \text{and} \quad \mathrm{w} = \frac{\Delta\phi^2}{2} \mathrm{b}^2.$$

Because v and w are both linear functions of which is equal to zero at the peak of the X-ray spectrum, the exponential is equal to one for $\omega = \omega_x$. In addition, the factor $[\Delta\phi(\Delta\gamma/\gamma_0)]^2$ in the square root shows that the relative energy spread must be compared to the normalized laser pulse duration, which is equivalent to the number of electromagnetic wiggler periods; this indicates that to increase the X-ray spectral brightness by lengthening the drive laser pulse, the requirement on the electron beam energy spread becomes increasingly stringent. Figure 5 illustrates the effects of energy spread, which are seen to symmetrically broaden the scattered X-ray spectrum and lower the peak intensity.

2.3. Emittance

We now turn our attention to the influence of the electron beam emittance:

$$\begin{aligned} &S_\varepsilon(\omega,\gamma_0,\Delta\gamma,\theta,\varphi_0,\Delta\varphi) \\ &\quad \simeq \frac{1}{\sqrt{\pi}\Delta\varphi} \int_0^{2\pi} S_\gamma(\omega,\gamma_0,\Delta\gamma,\theta-\delta,\varphi_0+\delta) \\ &\qquad \times \exp\left[-\left(\frac{\delta}{\Delta\varphi} \right)^2 \right] d\delta, \end{aligned} \tag{49}$$

where the spread of incidence angle is given in terms of the beam emittance ε, and radius r_b, by $\Delta\varphi = \varepsilon/\gamma_0 r_b$, and where φ_0 is the mean incidence angle, defined by the laser and electron beams. Again, the normalization constant is given by

https://doi.org/10.1017/S0263034604223059 Published online by Cambridge University Press

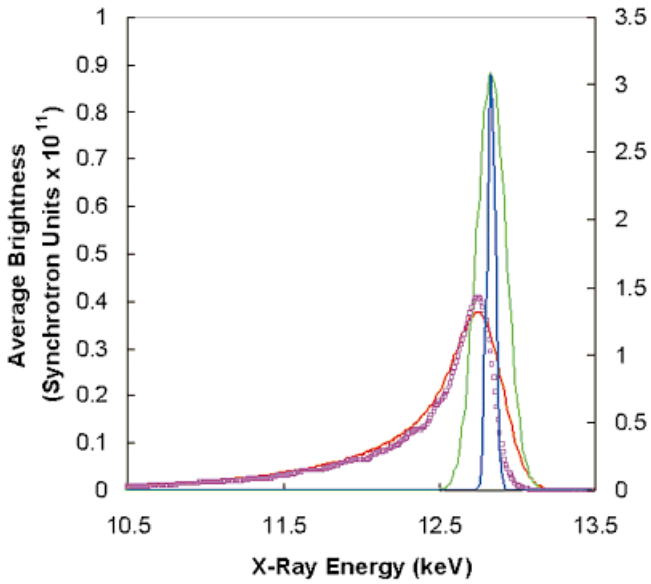

Fig. 5. A low energy, high repetition rate example, illustrating the broad potential capabilities of Compton scattering X-ray sources. On-axis X-ray spectral brightness for a cold beam (blue, right scale), $\Delta\gamma/\gamma_0 = 0.5\%$ (green), $\varepsilon = 1\ \pi$-mm·mrad (red), and three-dimensional computer simulations (red squares). The beam energy is 22.75 MeV, the bunch charge is 0.5 nC, and its duration is 1 ps; the laser wavelength is $\lambda_0 = 800$ nm ($Ti:Al_2O_3$), the laser pulse energy is 50 mJ, $w_0 = r_b = 10\ \mu$m cylindrical focus, $\varphi_0 = 180°$, $A_0 = 0.17$, and the overall repetition rate of the system is 1 kHz. The synchrotron units correspond to photons/(0.1% bandwidth $\times$ mm^2 $\times$ mrad^2 $\times$ s).

$$\int_0^{2\pi} \exp\left[-\left(\frac{\delta}{\Delta\varphi}\right)^2\right] d\delta \simeq \sqrt{\pi}\Delta\varphi, \tag{50}$$

provided that $\Delta\varphi \ll 1$.

In Eq. (49), we note the important geometrical correction term, $\theta - \delta$, which corresponds to the fact that the scattering angle is measured with respect to the initial electron velocity. The effect of emittance are illustrated in Figure 5, and are found to be independent of φ_0. Considering the on-axis X-ray spectral line, it is clear that emittance both asymmetrically broadens the spectrum and decreases the peak spectral brightness; near head-on collisions, a low energy tail develops because the maximum Doppler shift corresponds to $\delta \simeq 0$: Other electrons produce a smaller upshift, thus contributing to the lower energy photon population seen in Figure 5.

Returning to the cold, one-dimensional spectral brightness, the integral over a Gaussian distribution of incidence angle can be performed analytically, provided that the spectral density is approximated by the exponential of a biquadratic polynomial (Gradshteyn & Ryzhik, 1980, Eqs. 3.923, 3.924, and 3.323.3):

$$\int_0^\infty e^{-\mu x^4 - 2\nu x^2} dx = \frac{1}{4}\sqrt{\frac{2\nu}{\mu}} \exp\left(\frac{\nu^2}{2\mu}\right) \bar{K}_{1/4}\left(\frac{\nu^2}{2\mu}\right), \tag{51}$$

where $\bar{K}_{1/4}$ is defined in terms of Bessel functions of fractional order

$$\bar{K}_{1/4}\left(\frac{\nu^2}{2\mu}\right) = I_{-1/4}\left(\frac{\nu^2}{2\mu}\right) - \frac{\nu}{|\nu|} I_{1/4}\left(\frac{\nu^2}{2\mu}\right). \tag{52}$$

Because $\omega f(\gamma, \theta, \varphi)$ is a slow-varying function of the incidence angle, we can seek an approximate expression for the cold spectral density of the form

$$\begin{aligned} &S_0(\omega, \gamma, \theta - \delta, \varphi + \delta) \\ &\quad \simeq \omega f(\gamma, \theta, \varphi) \exp[-\mu(\omega, \gamma, \theta, \varphi)\delta^4 \\ &\qquad - 2\nu(\omega, \gamma, \theta, \varphi)\delta^2 + \lambda(\omega, \gamma, \theta, \varphi)]. \end{aligned} \tag{53}$$

The constant term is obtained by taking $\delta = 0 : \lambda(\omega, \gamma, \theta, \varphi) = -(\Delta\phi^2/2)[\chi(\omega, \gamma, \theta, \varphi) - 1]^2$; the other coefficients are derived using $\cos\delta \simeq 1 - (\delta^2/2!) + (\delta^4/4!)$, and $\sin\delta \simeq \delta - (\delta^3/3!)$. We then find that

$$\mu = \frac{\Delta\phi^2}{2} \frac{\mu_1 + \mu_2}{(\gamma - u\cos\varphi)^4}$$

and

$$2\nu = \frac{\Delta\phi^2}{2} \frac{\nu_1 - \nu_2}{(\gamma - u\cos\varphi)^4},$$

with

$$\mu_1 = (\gamma - u\cos\varphi)^2 \left\{ \begin{array}{l} \dfrac{u}{12}(\cos\varphi - \cos\theta) \\ \times[\gamma(\omega - 1) + u(\cos\varphi - \omega\cos\theta)] \\ -\dfrac{u^2}{3}(\omega\sin\theta + \sin\varphi)^2 \\ +\dfrac{u^2}{4}(\cos\varphi - \omega\cos\theta)^2 \end{array} \right\},$$

$$\mu_2 = [\omega(\gamma - u\cos\theta) - \gamma + u\cos\varphi]^2 \times \left[\frac{u}{12}\cos\varphi(\gamma - u\cos\varphi) + \frac{u^2}{3}\sin^2\varphi - \frac{u^2}{4}\cos^2\varphi\right],$$

$$\nu_1 = (\gamma - u\cos\varphi)^2 \left\{ \begin{array}{l} u^2(\omega\sin\theta + \sin\theta)^2 \\ -u(\cos\varphi - \omega\cos\theta)[\gamma(\omega - 1) \\ +u(\cos\varphi - \omega\cos\theta)] \end{array} \right\},$$

$$\nu_2 = [u\cos\varphi(\gamma - u\cos\varphi) + u^2\sin^2\varphi] \times [\omega(\gamma - u\cos\theta) - (\gamma - u\cos\varphi)]^2. \tag{54}$$

This result is compared to a full three-dimensional numerical simulation in Figure 5; the agreement is excellent. Note that to include both the effects of energy spread and emittance, the analytical results given in Eqs. (51) and (53) are multiplied by the energy spread degradation factor, as measured at the peak of the cold spectrum:

https://doi.org/10.1017/S0263034604223059 Published online by Cambridge University Press

$$S_\varepsilon \simeq \frac{\omega_x \mathrm{f}(\gamma_0,\theta,\varphi_0)}{\sqrt{1+\frac{1}{2}\left(\Delta\phi\,\frac{\Delta\gamma}{\gamma_0}\right)^2\left[\frac{\omega_x}{\gamma_0^2}\,\frac{\cos\varphi_0-\cos\theta}{(1-\cos\varphi_0)^2}\right]^2}}$$

$$\times\,\frac{\omega \mathrm{f}(\gamma_0,\theta,\varphi_0)}{2\sqrt{\pi}\Delta\varphi}\sqrt{\frac{2\nu}{\mu}}\exp\left(\frac{\nu^2}{2\mu}+\lambda\right)\bar{\mathrm{K}}_{1/4}\left(\frac{\nu^2}{2\mu}\right). \quad (55)$$

To summarize, we find that the spectral brightness, which is a delta-function for a single electron, is broadened by a number of factors: First, the finite laser pulse bandwidth yields a minimum spectral width, as the electron beam is illuminated by a photon distribution containing different colors; next, the energy spread of the electron beam also contributes to the broadening of the X-ray spectral brightness because the different electron energies translate into varying Doppler upshifts; finally, emittance contributes an asymmetric broadening toward low X-ray energies due to the tilt distribution of the X-ray cones radiated by the focusing electrons: Part of the on-axis radiation is actually contributed by lower energy photons radiated off-axis by electrons with finite transverse velocity. We also note that the three-dimensional focusing of the laser further increases the width of the X-ray spectrum by contributing a distribution of incidence angles. The X-ray phase space is a convolution of both the electron and laser beams phase space.

3. EXPERIMENTAL SETUP

The PLEIADES facility comprises three major subsystems: a TW-class CPA laser, a high-brightness electron linear accelerator, and the X-ray interaction region and diagnostics. In this section, each subsystem is described in detail, and their performance is assessed within the overall context of a bright, picosecond, tunable, hard X-ray source. The overall experimental repetition rate of the system is 10 Hz, and is limited by the available average pump power for the various lasers used at PLEIADES.

3.1. Laser system

The main laser system used for these experiments, which is known as the FALCON laser, is a Ti:Al_2O_3 CPA system capable of producing over 1 J of uncompressed light near 820 nm. The laser system front end is a compact C20s Ti:Al_2O_3 oscillator from Femtosource, which produces 30-fs pulses with a bandwidth of 36 nm centered at 815 nm. This mirror-dispersion-controlled Kerr-lens mode-locked laser also serves as the master clock for the entire experimental facility: A photodiode monitors the output pulse train of the oscillator, and that signal is compared to a 81.557-MHz reference signal from a stabilized crystal oscillator in a Time-Bandwidth CLX-1000 timing stabilizer. This box controls a picomotor and a piezoelectric crystal attached to the end mirror of the oscillator cavity, and adjusts the cavity length to keep the oscillator frequency stable. The photodiode signal is also filtered to produce a sinusoidal waveform that is frequency multiplied in a phase-locked dielectric resonant oscillator to 2.8545 GHz, which is then used to drive the rf amplifier and klystrons for the linear accelerator, ensuring phase locking between the laser and electron systems.

The oscillator pulses are stretched to 680 ps in an all-reflective parabolic-mirror based expander (Banks *et al.*, 2000). The pulse train is then split with a dielectric beam splitter into two beams, with 30% of the light being coupled into a fiber to seed the photoinjector laser, and the remaining 70% used to seed the FALCON laser. Because the same oscillator pulse train seeds both laser systems, minimal timing jitter between the systems is assured.

In the FALCON laser, the oscillator pulses are amplified to an energy of 7.3 mJ in a standard linear regenerative amplifier cavity, pumped with 45 mJ of 532 nm light produced by a frequency-doubled, flashlamp-pumped, Q-switched Nd:YAG Spectra-Physics GCR-190 laser. Following the regenerative amplifier is a 4-pass amplifier, which is pumped with the remaining 212 mJ of light from the GCR-190. The infrared input into the amplifier is monitored by two cameras, imaging the near and far field spots of the beam. A closed loop control system adjusts the pointing and centering of the beam via stepper motors on two mirrors to maintain alignment into the amplifier. The output energy of this amplifier is 68 mJ. This beam is then sent into a second 4-pass amplifier, which also has a closed-loop feedback system to maintain input alignment. This amplifier is pumped by 2.3 J of 532-nm light produced by a frequency-doubled, flashlamp-pumped, Q-switched Nd:YAG Spectra Physics QuantaRay PRO-350 laser as well as a 1-J, 532-nm, Q-switched Nd:YAG pump laser manufactured by Continuum, and produces 1.2 J of uncompressed IR light.

The amplified light beam is expanded and collimated to a $1/e^2$ radius of 42 mm; the beam is then relay imaged over 52 m, using two telescopes, to a vacuum chamber near the accelerator system, where it is compressed in a double-pass grating compressor. A frequency-resolved, optically gated GRENOUILLE system (O'Shea *et al.*, 2001, 2002) is used to measure the compressed pulses at low power, and yields a pulse length of 54 fs IFWHM, with a relative phase retrieval error of 0.006, as illustrated in Figure 6. The compressed pulse then propagates 20 m to the final focusing optics, currently an *f*:25 off-axis parabola. The loss through the transport and compressor is 45%, leaving up to 540 mJ available in the interaction region.

3.2. Linear accelerator

The high-brightness electron beam used to generate X rays at PLEIADES is produced by the Lawrence Livermore National Laboratory 100-MeV linear electron accelerator, which has been substantially upgraded to meet the stringent emittance and timing jitter requirements necessary for efficient Compton scattering. The most significant upgrade was the installation of a new photoinjector at the front end of the accelerator, as an alternative to the preexisting thermionic

https://doi.org/10.1017/S0263034604223059 Published online by Cambridge University Press

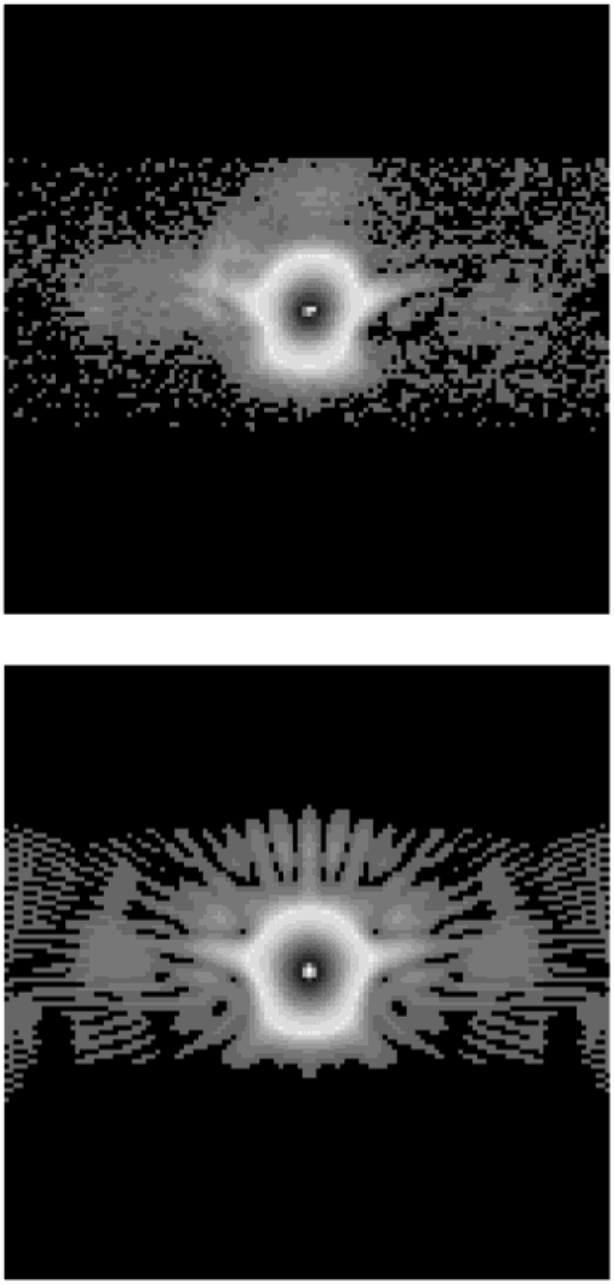

Fig. 6. GRENOUILLE measurements of the FALCON laser pulse duration. Top: Experimental data. Bottom: Retrieved data, with a phase error of 0.006; the corresponding IFWM of the pulse is 54 fs.

injector. In the S-band photoinjector, a high charge (nC), picosecond electron bunch is produced via the photoelectric effect when a UV laser pulse illuminates the photocathode. The photoemission threshold for the Cu photocathode is 266 nm, but this value is significantly relaxed by the strong Schottky effect induced by the 80–100-MeV/m rf field applied to the photocathode; indeed, the central wavelength of the UV beam produced after frequency tripling is only 269 nm, but this is sufficient to obtain a quantum efficiency varying between 8×10^{-6} and 2×10^{-5}, depending on the laser injection phase.

As the UV laser system driving the photoinjector is seeded by the same laser oscillator used for the FALCON laser, the injection time of the electrons into the linear accelerator can be synchronized to within 1 ps to both the FALCON laser pulse and the S-band rf fields that energize the linear accelerator. A second major benefit of the photoinjector technology is that it allows for electron beams with much higher current densities. For a given extracted charge, this gives a much smaller initial spot, and a correspondingly lower emittance, as well as a high (∼100 A) current. Additionally, the accelerating gradients in a photoinjector (∼100 MeV/m) are generally much greater than those in thermionic guns, thus limiting the detrimental effects of space-charge-induced emittance growth that occur at low energy, before the beam becomes relativistic.

The photocathode UV laser system was installed as close as practical to the linear accelerator and seeded through a 50-m, single-mode fiber with 30% of the light that is split off from the main oscillator pulse. After coupling and transport losses, the seed light has an average power of 7.3 mW, or 90 pJ per pulse, which is coupled into a linear regenerative amplifier cavity. The Ti:Al_2O_3 crystal in this amplifier is pumped with 50 mJ of 532-nm light from a frequency-doubled, flashlamp-pumped, Q-switched Nd:YAG DCR-2 laser. The end mirror leakage of this amplifier is monitored with a fast photodiode, which provides a trigger timing signal for the streak camera and other diagnostics, which are discussed later. This system produces 5.9-mJ IR pulses at 10 Hz. Following the regenerative amplifier is a bow-tie configuration 4-pass power amplifier, similar to the two discussed for the FALCON system. The Ti:Al_2O_3 crystal is pumped with the 280 mJ of laser light from the DCR pump that is not sent to the regenerative amplifier, and amplifies the output of the regenerative amplifier up to the 90-mJ level. Again, this amplifier has an active pointing and centering system used to align the regenerative amplifier light pulses as they are injected into the final amplification stage.

The light from the 4-pass is then sent into a grating compressor. The pulse is not fully compressed to its transform limit; instead, a UV pulse length of approximately 3 ps rms is used to illuminate the photocathode. This is because detailed simulations of the electron beam in the photoinjector clearly show that the best quality beams, as evaluated in terms of energy spread and emittance, are produced when using UV laser pulses with durations of a few picoseconds to generate photoelectrons. In turn, this results from the Coulomb repulsion of the electrons, which are initially created at rest: As the laser pulse gets shorter, the electron density increases until space-charge forces begin severely degrading the electron beam transverse and longitudinal emittance. This longer pulse also has the advantage of minimizing the effects on the laser pulse temporal structure resulting from the residual cubic phase distortions introduced by the 50-m fiber that transports the laser oscillator pulse to the UV photocathode laser system. However, it should also be noted that the broadband nonlinear frequency

https://doi.org/10.1017/S0263034604223059 Published online by Cambridge University Press

tripler used to produce UV from the IR pulses is a challenging component to optimize because the residual chirp of the partially compressed pulse introduces distortions that make phase-matching difficult.

Following compression, the pulse is first frequency doubled in a Type I BBO crystal, then tripled in a second Type I BBO crystal to 269 nm. A special wave plate is used between the harmonic crystals, which rotates the polarization of the second harmonic by a half wave to align it with the fundamental for sum-frequency mixing. Generally, about 1.2 mJ of UV light is available; however, to prevent damage to the cathode in the photoinjector, the system is often turned down to provide only about 500 μJ of light at the tripler output. This UV pulse is then clipped with an aperture to a diameter of 2 mm to provide a hard-edged UV spot, which further improves the emittance of the photoinjector. The aperture plane is relay imaged 50 m to the photoinjector cathode. The UV pulse width is measured at 3 ps rms with a 500-fs-resolution streak camera using a multiphoton Au photocathode.

The rf photoinjector used to produce the electron beam for PLEIADES is based on a 1.6-cell standing-wave geometry (Le Sage *et al.*, 2001). A pulsed S-band (2.8545 GHz) rf input with 7-MW peak power and 3-μs duration produces a peak axial electric field of up to 100 MV/m that accelerates the electrons to 5 MeV. Focusing solenoids are employed in the photoinjector to preserve the transverse emittance (Carlsten, 1989; Reiser, 1994; Wiedemann, 1999) of the electron bunch, help match the electron beam into the accelerating sections, and to implement emittance compensation (Carlsten, 1989). The gun currently operates with a more conservative accelerating gradient of 80 MV/m to avoid any possible damage due to rf arcing, which also leads to lower quantum efficiency on the photocathode.

The electron bunch charge is determined by the pulse parameters of the UV laser and the quantum efficiency of the photocathode. The 269-nm laser pulse is imaged to a 1–2-mm spot on the Cu photocathode, where the axial rf field is nearly maximal; under these operating conditions, electrons are produced with a typical quantum efficiency of approximately 8×10^{-6} electrons/photon, which yields an electron bunch charge between 250 and 350 pC, as shown in Figure 7 (top).

The electron bunch length is a function of the laser pulse duration, bunch charge, and accelerating voltage, and is typically a few picoseconds long, although bunch lengths as short as 300 fs have been measured using coherent transition radiation, by operating at reduced bunch charge and using velocity compression. As mentioned earlier, because both the UV photocathode laser, which is directly responsible for producing the electron bunch, and the FALCON drive laser are seeded from the same oscillator pulse train, the timing of the electron beam is well synchronized to the laser pulse that it collides with to produce X rays.

The beam generated by the photoinjector is then coupled into the 100-MeV linear electron accelerator (Fultz & Whitten, 1971), where it is accelerated to energies ranging between 20 and 100 MeV by four 1.8-m, SLAC-type traveling-wave accelerating sections.

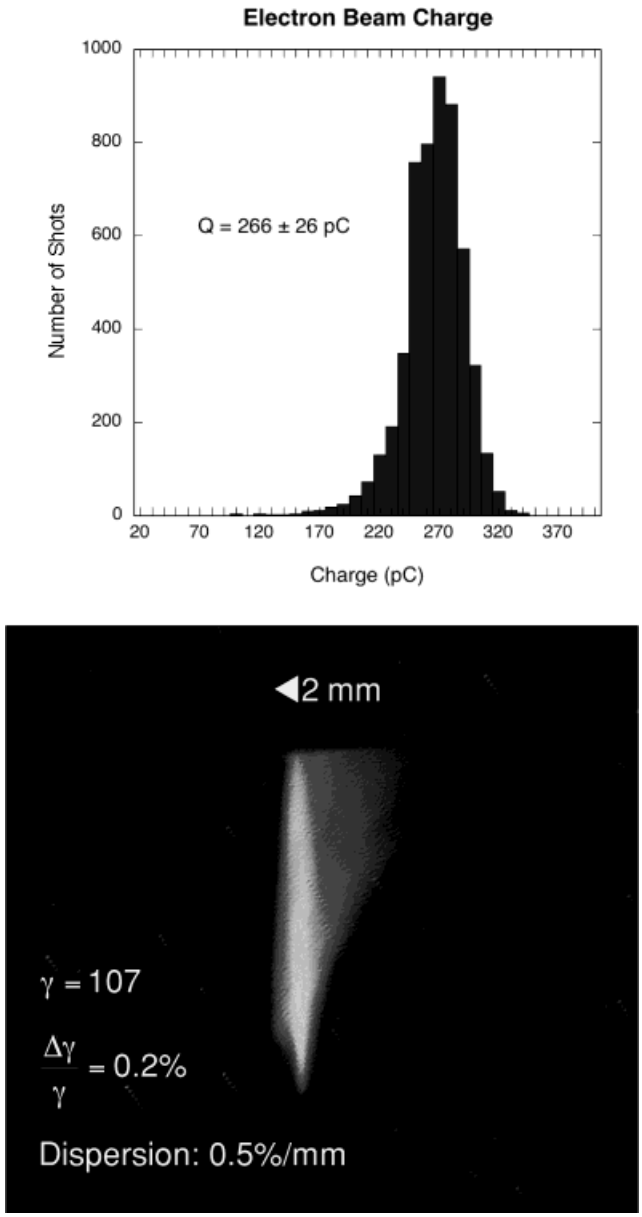

Fig. 7. Top: Measurement of the bunch charge extracted from the S-band rf gun. Bottom: Energy spectrum of the electron beam, measured using a 30° dipole with a dispersion of 0.5%/mm at 60 MeV.

After propagating through the interaction area, as shown in Figure 8, the electron beam is deflected by a 30°-bend dipole magnet that separates the bunch from the scattered X rays, which propagate in the same direction as the electrons. This dipole also serves as a spectrometer, yielding detailed measurements of the electron beam energy and energy spread, which is as low as $\Delta\gamma/\gamma \simeq 0.2\%$, as shown in Figure 7 (bottom). Following the energy spectrometer, the electron beam is stopped in a Cu collector that also serves as a calibrated Faraday cup, providing a measure of the elec-

https://doi.org/10.1017/S0263034604223059 Published online by Cambridge University Press

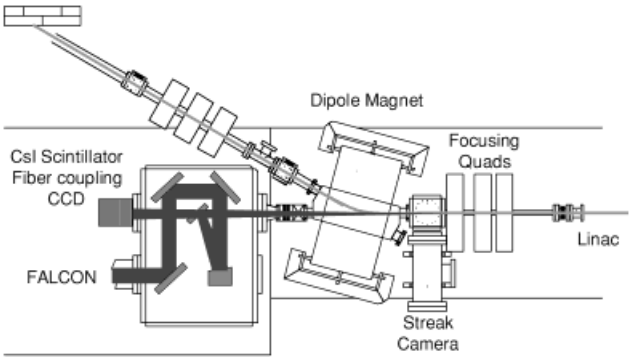

Fig. 8. Schematic of the interaction region, including some of the laser and electron beam optics, and diagnostics.

tron bunch charge. The electron collector is housed in a 10-cm-thick lead enclosure to minimize the effect of bremsstrahlung on the diagnostics.

3.3. Interaction region and interaction geometry

Two fundamental interaction geometries can be used to perform Compton scattering experiments: 180° (head-on) collisions, or 90° (side-on) interactions. Each approach has its own merits, as discussed below. The main advantage of a noncollinear geometry is that very short X-ray pulse lengths can thus be generated: In this case, the duration of the X-ray flash is equal, to first order, to the transit time of the laser pulse through the focused electron bunch. By comparison, in a collinear geometry with an ultrashort (<100 fs) laser pulse, the X-ray pulse duration is essentially that of the electron bunch, generally on the order of a few picoseconds. In a 90° interaction, the duration is a convolution of the laser pulse length and the electron beam diameter, and is only on the order of a few hundred femtoseconds.

However, the main disadvantages of a 90° interaction geometry are a lower X-ray flux, resulting from the fact that, for picosecond electron beams, the laser pulse only interacts with a small fraction of the electrons, or the considerably more stringent pointing and timing requirements. This can be studied more systematically by considering the variation of the X-ray dose as a function of the timing delay between the drive laser pulse and the electron bunch for different interaction geometries, as illustrated in Figure 9. Here, we consider a 100-mJ, 50-fs FWHM, 20-μm FWHM laser pulse interacting with a 1-nC, 2-ps FWHM, 20-μm FWHM, 5-mm·mrad emittance electron beam, and calculate the dose by integrating Eq. (21) over time for the laser photon density of a focusing wave given in Eq. (36) and summing over a distribution of electrons produced by the code PARMELA. In the case of 180° collisions, the X-ray dose as a function of delay varies essentially like the Lorentzian $1/[1 + (z/z_0)^2]$, which characterizes the diffraction of the laser beam; for the parameters quoted above, the FWHM of the X-ray dose produced as a function of the time between

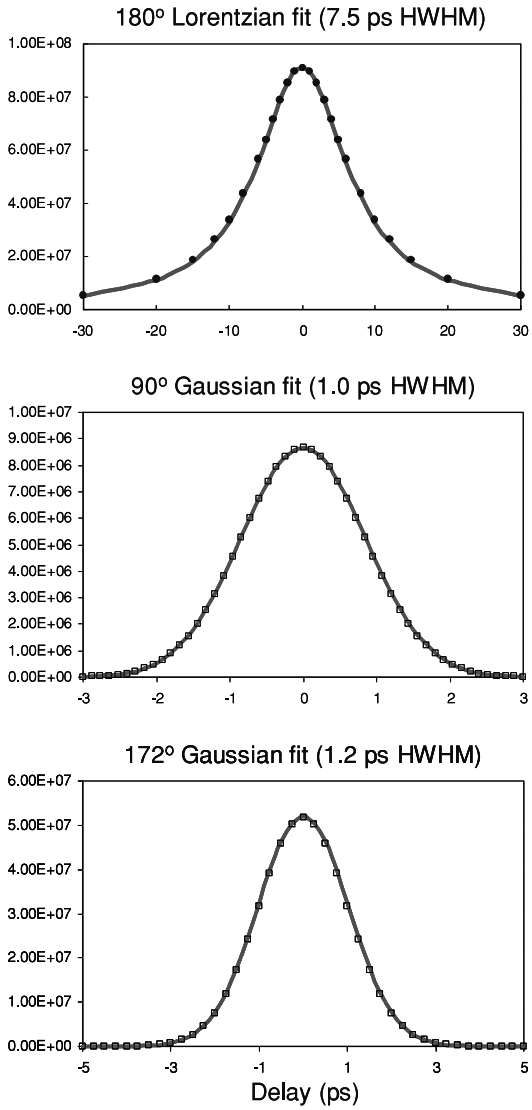

Fig. 9. Computer simulations of the X-ray dose as a function of the delay between the laser pulse and the electron bunch. The parameters used are as follows: laser pulse duration, 50 fs IFWHM; focal spot size, 20 μm IFWHM; laser pulse energy, 100 mJ; electron bunch duration, 2 ps FWHM; electron bunch charge, 1 nC; bunch focal spot size, 20 μm FWHM; normalized emittance, 2 mm·mrad.

the arrival of the laser pulse and the arrival of the electron bunch at the focus is $\Delta t = 15$ ps, which corresponds to a Rayleigh length $z_0 = c\Delta/2 = 2.25$ mm, in close agreement with the theoretical value, $z_0 = \pi w_0^2/\lambda_0$, where $w_0 = \sqrt{2\ln(2)} \times \text{FWHM} = 23.6$ μm. This effect has been measured and is discussed in Section 4. For the same beams in a 90° geometry, the dose FWHM is only 2 ps, and the number of X rays produced drops by a factor of 10; furthermore, the profile is now Gaussian, reflecting the temporal shape of the electron bunch. Even at a shallow interaction angle of 172°, the interaction window drops to 2.3 ps. The much larger interaction window in the 180° geometry results from the fact that the Rayleigh range and beta function of the laser and electrons, respectively, are much longer than the actual

https://doi.org/10.1017/S0263034604223059 Published online by Cambridge University Press

bunch lengths. When the beams are collinear, delay simply translates into a longitudinal motion of the X-ray source, within the spatial volume defined by the two focusing ranges; furthermore, in that configuration, all the electrons are illuminated by the drive laser, provided the transverse beam sizes are similar, thus maximizing the X-ray dose. Because of the numerous aforementioned advantages of the 180° interaction geometry, this configuration was chosen for initial experiments; furthermore, for head-on collisions, the X-ray pulse duration is governed by the electron bunch length, which has been successfully compressed down to 300 fs rms; therefore, the 180° interaction geometry does not create any significant limitations for ultrafast X-ray experiments.

The layout of the PLEIADES interaction region is shown in Figure 8. The 480-mJ IR laser pulse is focused off a 60-in. focal length, 12° off-axis parabolic mirror. The focusing beam is then directed to the interaction region by a motor-controlled dielectric mirror, which allows for control of the transverse alignment of the laser focus at the interaction point. The spot is observed to have a $1/e^2$ waist radius of 36 μm (42.2 μm FWHM) along the polarization and a measured M^2 value of 1.6, as shown in Figure 10, whereas the $1/e^2$ waist radius and M^2 are equal to 28 μm and 1.2 across the polarization; the average $1/e^2$ radius is 32 μm, the average M^2 is 1.4. In this case, the Rayleigh range, which defines the interaction region in a 180° geometry, is $\langle z_0 \rangle = \pi \langle w_0^2 \rangle / \lambda_0 \langle M^2 \rangle = 2.86$ mm. After interaction with the electrons, the laser beam propagates down the linear accelerator beamline and dumps its energy in the walls as it expands after the focus.

The electron beam is focused by a set of quadrupole magnets with a magnetic field gradient of up to 15 T/m. To aid alignment at the focus, two cross-oriented dipole magnets steer the beam into this composite magnetic lens. Because the off-axis parabolic mirror that focuses the laser is fixed, the longitudinal position of the interaction region is set by the laser focus, and the longitudinal position of the electron beam waist is adjusted to the position of the laser focus using the electron focusing system. Measurements of the electron beam at the focus have shown a spot size $\sigma_x = \sigma_y = 27$ μm rms, a normalized horizontal emittance $\varepsilon_x = 3.5$ mm·mrad rms, and a normalized vertical emittance $\varepsilon_x = 11$ mm·mrad rms, which were measured using the standard quadrupole scan technique. Typical measurements are illustrated in Figure 11.

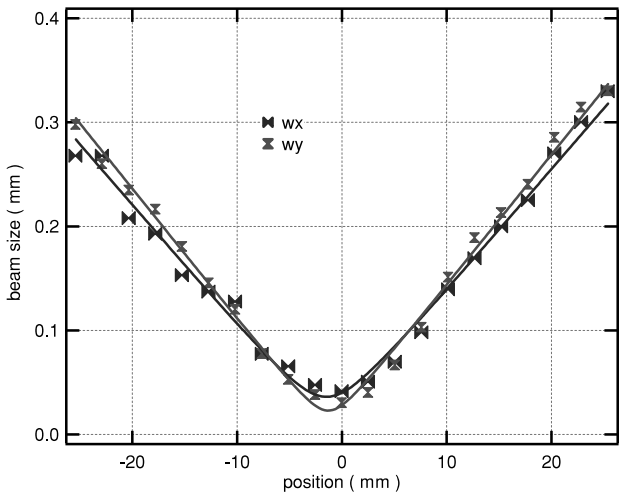

Fig. 10. Measurements of the FALCON laser M^2. The spot is observed to have a $1/e^2$ waist radius of 36 μm (42.2 μm FWHM) along the polarization and a measured M^2 value of 1.6, whereas the $1/e^2$ waist radius and M^2 are equal to 28 μm and 1.2 across the polarization.

Spatial alignment of the two focal spots is performed with the aid of an optically polished 0.3-in. Al cube. The cube is mounted on a three-axis translation stage with its faces oriented vertically normal to the beamline, and horizontally at 45° to the beamline. Because the laser beam reflects well from the surface, the focus at the surface of the cube can be imaged into a CCD camera. To avoid damaging the cube or camera, the IR laser pulse energy is reduced by a combination of turning off the pump lasers to the two 4-pass amplifiers and inserting neutral density filters to attenuate the beam by a factor of 10^8; special care was taken to ensure that this attenuation process did not significantly steer the laser pulse nor change its timing delay. When the electron beam strikes the cube, it produces OTR, which can also be imaged by the CCD camera. The vertical alignment of the two beams is then readily apparent, and the horizontal alignment is determined by positioning the cube such that both beams just hit the cube edge. Generally, the procedure is to place the cube at the laser focus, optimize the electron beam focus on the cube, and steer the laser beam laterally to align to the optimal electron beam position.

Temporal synchronization is far more complex than spatial alignment because the propagation times for the FALCON laser and the UV laser and electron beam, which are set by path lengths that are approximately 70 m long, must be matched to within a few picoseconds. There are three steps to the initial synchronization. First, a beam-current pickoff and an IR photodiode are used to determine the initial timing, to within a few hundred picoseconds. The electron beam propagating through the interaction area generates a short magnetic field pulse, which induces a voltage converted into a current pulse in the two 100-Ω junctions of the pickoff. The generated signal is then detected by an oscilloscope as ~150 ps FWHM pulses. Similar accuracy is obtained for the arrival time of the laser by using a fast infrared UHS 016 photodiode. By selecting a different oscillator pulse to switch into the FALCON regenerative amplifier, it is possible to get the electron and laser arrival time difference to less than 12 ns, the spacing between subsequent oscillator pulses. Second, for more accurate timing, we use a Nikon Nikkor 50-mm f/1.4 lens to image the OTR and the laser light reflected from the cube onto a 100-μm slit on an Imacon 500 Series streak camera. This camera uses an S20 photocathode with a quantum efficiency greater than

https://doi.org/10.1017/S0263034604223059 Published online by Cambridge University Press

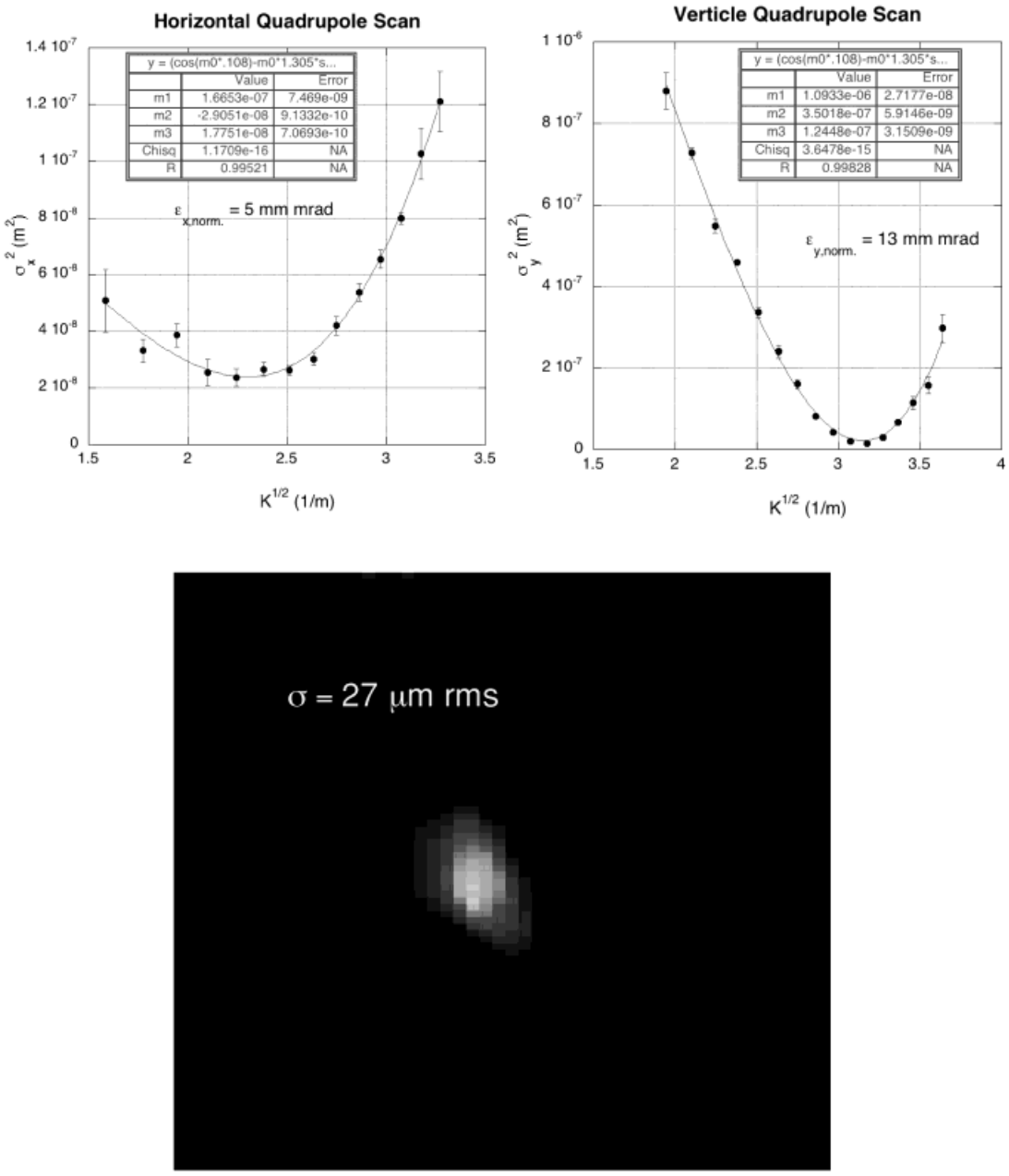

Fig. 11. Top: Quadrupoles scans used to determine the emittance of the electron bunch. In this specific case, the normalized horizontal emittance is 5 mm·mrad, and the vertical emittance is 13 mm·mrad. Improvements on the beamline tuning have produced emittances as low as 3.5 mm·mrad horizontally and 11 mm·mrad vertically. Bottom: Optical transition radiation image of the focused electron beam; $\sigma_x = \sigma_y = 27$ μm rms, at 57 MeV.

5% over visible wavelengths, which makes simultaneous streaking of the OTR and the drive laser light possible. Using a combination of this streak camera and the current pickoff and photodiode signals, the laser and electron timing are brought to within a few tens of picoseconds by manually sliding the retro-reflecting roof mirror in the FALCON compressor along a 2-m rail. Because this mirror is located between the second and third grating strike in the compressor, its position does not have a significant effect on the compressed pulse. The third and final stage of temporal synchronization is performed using the streak camera at its highest sweep speed, 18.7 ps/mm, which provides a temporal resolution of 2 ps, limited by the spacing on the microchannel plate that is used as an amplifier for the streak camera output phosphor screen and by the entrance slit size. Using this signal and a motorized stage under the same roof mirror in the compressor, the laser and electron beam arrival times can be synchronized to within the resolution of the streak camera. This measurement also gives the relative timing jitter, which is found to be below the streak camera

https://doi.org/10.1017/S0263034604223059 Published online by Cambridge University Press

resolution. Attempts at further optimizing the timing by maximizing the X-ray signal directly as a function of the delay between the pulses yield no improvement, indicating that the temporal overlap achieved with the 2-ps resolution of the streak camera is, as expected, sufficient for the 180° interaction geometry.

4. X-RAY MEASUREMENTS AND COMPARISON WITH THEORY

In this section, a number of important X-ray measurements are presented and compared with theory, including the X-ray dose and energy-integrated angular distribution, X-ray dose as a function of delay between the laser and electron beams, determination of the X-ray spectrum scattered on-axis, and *K*-edge radiography in Ta, Er, and other high-*Z* elements.

4.1. X-ray dose and energy-integrated angular distribution

A variety of diagnostics are available to detect the X rays produced by Compton scattering. The primary diagnostic is an X-ray CCD, which comprises a 140-μm-thick CsI scintillator, doped with Tl, that is coupled by an optical fiber bundle to a Princeton Instruments 16-bit, 1340×1300 pixel CCD chip, with a demagnification of 3:1. The chip size is 2.54×2.54 cm^2, which provides a detection surface of 7×7 cm; the effective pixel size is 60×60 μm^2. The scintillator, which is protected by a 0.5-mm-thick Be filter, provides a photon detection quantum efficiency of 0.4 at 60 keV. The X-ray CCD was calibrated using a 59.5 keV Am_{241} radioisotope source. The source itself is calibrated using a single-photon counting Ge(Li) detector with a quantum efficiency for the energies of interest that is close to 100%. The measurement results indicate 0.12 counts/keV at 59.5 keV; from that calibration point, the response of the X-ray CCD can be extrapolated using the X-ray absorption in CsI from the NIST database:

$$R(E) = R(E_0)\,\frac{1-\exp[-\rho_{\mathrm{CsI}}\mu_{\mathrm{CsI}}(E)\Delta_{\mathrm{CsI}}]}{1-\exp[-\rho_{\mathrm{CsI}}\mu_{\mathrm{CsI}}(E_0)\Delta_{\mathrm{CsI}}]}, \qquad (56)$$

where $\Delta_{\mathrm{CsI}} = 140$ μm is the scintillator thickness, $E_0 = 59.5$ keV is the calibration energy, $\rho_{\mathrm{CsI}} = 4.51$ g/cm^3 is the density of CsI, and the data for the mass attenuation coefficient, $\mu(E)$, measured in square centimeters per gram can be found at http://physics.nist.gov/PhysRefData/FFast/html/form.html.

In addition to the response of the CsI(Tl) scintillator, the transmission of the X-ray through a $\Delta_{\mathrm{BK7}} = 12.7$-mm-thick BK7 mirror tilted at 40° must be taken into account: As seen in Figure 8, the X rays produced at the interaction point propagate through this final folding mirror before detection. BK7 is a Crown glass containing 67% SiO_2, 12.6% B_2O_3, 8.1% Na_2O, and 12.3% K_2O; the percentages are given in terms of weight, and the X-ray mass attenuation coefficients add up linearly, provided the relative compositional weight fractions and atomic weights are properly taken into account; the mass density of BK7 is 2.51 g/cm^3. Finally, the multilayer dielectric coating used to reflect the focusing IR beam is extremely thin, and does not significantly absorb the X rays.

Although the number of photons produced in a single shot is sufficient to be detected by the X-ray CCD, better statistics are obtained for integration times of 10 s, representing 100 shots. It is found that the pointing stability of the X-ray beam is very good, because no significant broadening of the angular X-ray distribution can be detected over long integration times.

Figure 12 shows a typical X-ray image captured by the CCD. The effect of the horizontal and vertical electron beam emittance is striking: For a cylindrical spot, the electron beam diverges faster in the vertical direction, and the X rays, which are primarily scattered along the individual velocities of the electrons due to the Doppler effect, clearly reflect the electron beam transverse phase space.

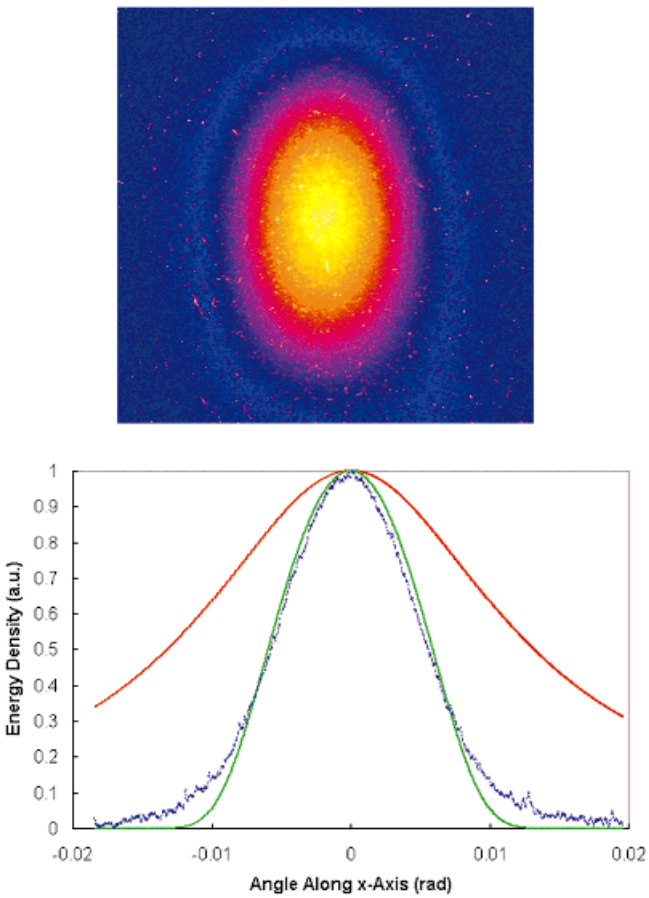

Fig. 12. Top: False color image of the X-ray angular energy distribution captured by the CCD over 10 s of integration. Bottom: Lorentzian distribution $(1+\gamma^2\theta^2)^{-1}$ along the direction of polarization, for $\gamma = 107$ (red); experimental data (blue dots); and theoretically calculated pattern after transmission through the BK7 mirror, taking into account the energy-dependent response of the CCD (green).

https://doi.org/10.1017/S0263034604223059 Published online by Cambridge University Press

A closer examination and analysis of the angular distribution of X-ray energy captured by the CCD provides valuable information on the X-ray phase space, and is outlined in the following paragraphs. The X-ray source can be characterized by the number of photons scattered per unit frequency and solid angle in a single shot, $d^2N_x/d\omega_x d\Omega_x$, which is a quantity that can be determined theoretically using either of the two codes mentioned in Section 2. The spectral energy density radiated is simply given by

$$S_x(\hbar\omega_x, \hat{\mathbf{n}}_x) = \frac{d^2N_x}{d\omega_x d\Omega_x}\hbar\omega_x, \tag{57}$$

where $\hat{\mathbf{n}}_x$ is the direction of observation. To obtain a relation between the X-ray CCD signal and the spectral energy density at the source, propagation through various materials must be taken into account, as well as the response of the CCD. Taking into account the BK7 mirror and a $\Delta_{\rm Al} = 1$-mm Al window, we first obtain the transmitted spectral density,

$$\frac{d^2N_x(\hbar\omega_x, \hat{\mathbf{n}}_x)}{d\omega_x d\Omega_x}\hbar\omega_x T_{\rm BK7}(\hbar\omega_x)T_{\rm Al}(\hbar\omega_x),$$

$$T_{\rm BK7}(\hbar\omega_x) = \exp\left[-\rho_{\rm BK7}\mu_{\rm BK7}(\hbar\omega_x)\frac{\Delta_{\rm BK7}}{\cos(40^\circ)}\right],$$

$$T_{\rm Al}(\hbar\omega_x) = \exp[-\rho_{\rm Al}\mu_{\rm Al}(\hbar\omega_x)\Delta_{\rm Al}]. \tag{58}$$

The CCD yields an energy-integrated response, which can be calculated by taking the integral of the product of the transmitted spectral density and the CsI response over all frequencies and dividing by the number of shots:

$$IR(\hat{\mathbf{n}}_x) = \frac{1}{n}\int_0^\infty \frac{d^2N_x(\hbar\omega_x, \hat{\mathbf{n}}_x)}{d\omega_x d\Omega_x}\hbar\omega_x T_{\rm BK7}(\hbar\omega_x)T_{\rm Al}(\hbar\omega_x)R(\hbar\omega_x^0)$$
$$\times\frac{1-\exp[-\rho_{\rm CsI}\mu_{\rm CsI}(\hbar\omega_x)\Delta_{\rm CsI}]}{1-\exp[-\rho_{\rm CsI}\mu_{\rm CsI}(\hbar\omega_x^0)\Delta_{\rm CsI}]}d\omega_x; \tag{59}$$

on a given X-ray CCD pixel, this translates into a signal

$$s_{ij} \simeq \Delta\Omega \times IR(\hat{\mathbf{n}}_x = \hat{\mathbf{x}}\Delta\theta_i + \hat{\mathbf{y}}\Delta\theta_j),$$

$$\Delta\Omega = \left(\frac{60}{L}\right)^2 \mu\text{rad}^2,$$

$$\Delta\theta_i \simeq i\left(\frac{60}{L}\right)\mu\text{rad}, \qquad \Delta\theta_j \simeq j\left(\frac{60}{L}\right)\mu\text{rad}. \tag{60}$$

Here, we have used the pixel size and the distance from the source, L, which is equal to 1.5 m, in the specific case of Figure 12, and the fact that for small angles $\sin\theta \simeq \theta$ and $\cos\theta \simeq 1-(\theta^2/2) \simeq 1$. The indices i and j refer to the pixel position, with $i = j = 0$ on-axis. Integration over all solid angles, or summation over all pixels, yields the X-ray dose, which is approximately 3×10^6. For typical X-ray runs, the maximum dose per shot is approximately 20% larger than the average dose per shot, showing good overall system stability.

Additional information is contained in the pixel signal distribution, and can be understood by considering Figure 13: Here, we have plotted the spectrum at various angles ranging from 0 to 12 mrad, both along the laser polarization (top), and across it (center). It is clear that the radiation pattern is asymmetric, as well as the spectral content; this is due to both the asymmetric emittance and to the polarization. Along the laser polarization, the spectrum downshifts rapidly with angle, leading to a very strong attenuation in the BK7 mirror and a narrow radiation pattern, as illustrated in Figure 12 (bottom), which shows superb agreement between the theoretical angular energy distribution, taking into account

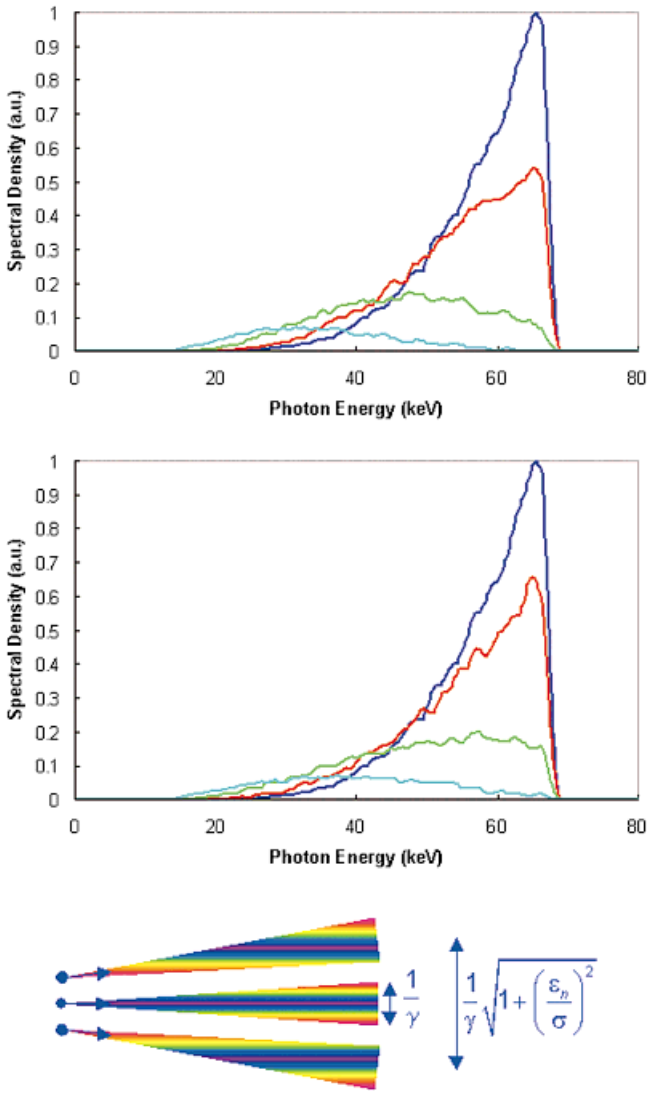

Fig. 13. Top: Energy spectra at 4 different values of θ_x; 0 mrad (dark blue), 4 mrad (red), 8 mrad (green), 12 mrad (aqua). Center: Energy spectra at 4 different values of θ_y; 0 mrad (dark blue), 4 mrad (red), 8 mrad (green), 12 mrad (aqua). The electron beam parameters correspond to the experimental conditions in Figure 12. Bottom: Illustration of the spectral and angular broadening effects induced by the electron beam emittance.

https://doi.org/10.1017/S0263034604223059 Published online by Cambridge University Press

the BK7, and the measured data. Note that the red curve, which shows the Lorentzian energy distribution $1/(1 + \gamma^2\theta^2)$, is much wider than the recorded data; this is because the emittance, polarization, and transmission effects are not taken into account by this simple model. Returning to our discussion, we see that across the laser polarization, the downshift is much slower because of the high-energy contribution of electrons with a high angle of incidence due to the emittance, as shown schematically in Figure 13 (bottom); this leads to better transmission through the BK7, and to a highly asymmetric pattern on the CCD.

4.2. X-ray dose as a function of delay

The timing between the laser pulse and the electron bunch can be varied by using an optical delay line, and allows for measuring the scattered X-ray dose as a function of the synchronization between the two beams. Theoretically, the dominant effect for the 180° interaction geometry and the PLEIADES parameters, where the inverse beta function of the electron beam optics is much longer than the diffraction length of the laser and where the electron bunch duration is much longer than the laser pulse, is the Rayleigh range determined by the laser focusing optics and beam quality. For the specific measurements presented in Figure 14, $M^2 \simeq 1.45$, $w_0 \simeq 37$ μm, and the central laser wavelength is $\lambda_0 = 815$ nm, the dose is expected to vary as a Lorentzian

$$N_x(\Delta t) \propto \frac{1}{1 + (z/z_0)^2} = \frac{1}{1 + \left(\dfrac{c\Delta t \lambda_0 M^2}{\pi w_0^2}\right)^2} = \frac{1}{1 + (\Delta t/\tau)^2}, \tag{61}$$

with a HWHM equal to $\pi w_0^2/c\lambda_0 M^2 \simeq 12.1$ ps, which is superimposed to the experimental data on Figure 14; the agreement is quite good. The asymmetry probably results from the fact that the electron bunch carries more charge near its front end: When the collision occurs on the "upstream" side of the focus (right side in Fig. 14), the high-charge front of the bunch experiences a higher photon density than its low-charge tail; this situation is reversed for collisions occurring on the other side of the focus, which results in the observed difference in the number of scattered photons.

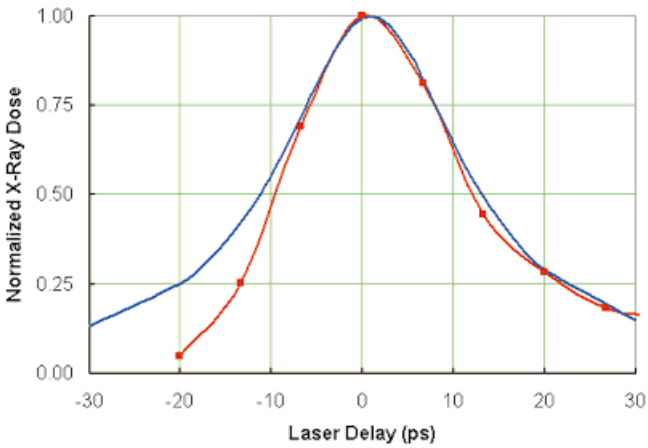

Fig. 14. Experimentally measured variation of the X-ray dose with the delay, Δt (red), and theoretically derived Lorentzian, $[1 + (\Delta t/\tau)^2]^{-1}$, where $\tau = \pi w_0^2/c\lambda_0 M^2 = 12.1$ ps.

4.3. On-axis X-ray spectrum

A number of different methods are available to determine the spectral content of the scattered X rays. In general, three distinct categories of diagnostics can yield spectral information: First and foremost, diffraction crystals can be used to match the well-known Bragg condition, $2d \sin\theta_B = \lambda_B$, where the so-called $2d$-spacing of the lattice is typically equal to a few angstroms; second, energy detectors, such as scintillators and X-ray diodes, can be operated in the single-photon counting regime, where a statistical analysis of the data can yield the X-ray spectrum; finally, the fact that X-ray attenuation in materials is generally a strong function of the photon energy can be used to infer the spectrum of a source. The results presented in this article were collected using the latter technique because, in its present configuration and for the diagnostics currently available, the two other approaches proved impractical: Because the X rays propagate through a relatively thick BK7 mirror, the signal is strongly attenuated for energies below 40 keV, and readily available crystals, such as Si (111) with a $2d$-spacing of 6.2712 Å, would yield very small Bragg angles or poor reflectivity. LiF (420) crystals, with $2d$-spacing of 1.801 Å, will be used in the near future to confirm the spectral measurements. On the other hand, in the present 180° degree geometry, the X-ray detectors are placed directly in the line of sight of the bremsstrahlung produced by the dark current in the linear accelerator, which results in background levels that are incompatible with the aforementioned single-photon counting technique. This problem will be mitigated by additional shielding, limiting the rf pulse duration in the linac, using two dipoles to offset the interaction region from the main linac axis, and by diffracting the X-ray signal away from the components producing background via bremsstrahlung and inner shell-edge fluorescence. In view of the above, the most robust technique was chosen to perform the initial spectral measurements: A series of 787-μm-thick Al plates was placed in front of the X-ray CCD, obscuring only half of the scintillator to normalize the transmission through a variable number of plates. The technique is illustrated in Figures 15 and 16, where 15 plates were used for an integration time of 10 s; a lineout then provides the value of the transmission for the on-axis spectrum. Repeating this measurement technique then yields the transmission as a function of the Al thickness.

Spectral information can then be retrieved by applying the analysis technique outlined in the following paragraphs. The transmission is given by

https://doi.org/10.1017/S0263034604223059 Published online by Cambridge University Press

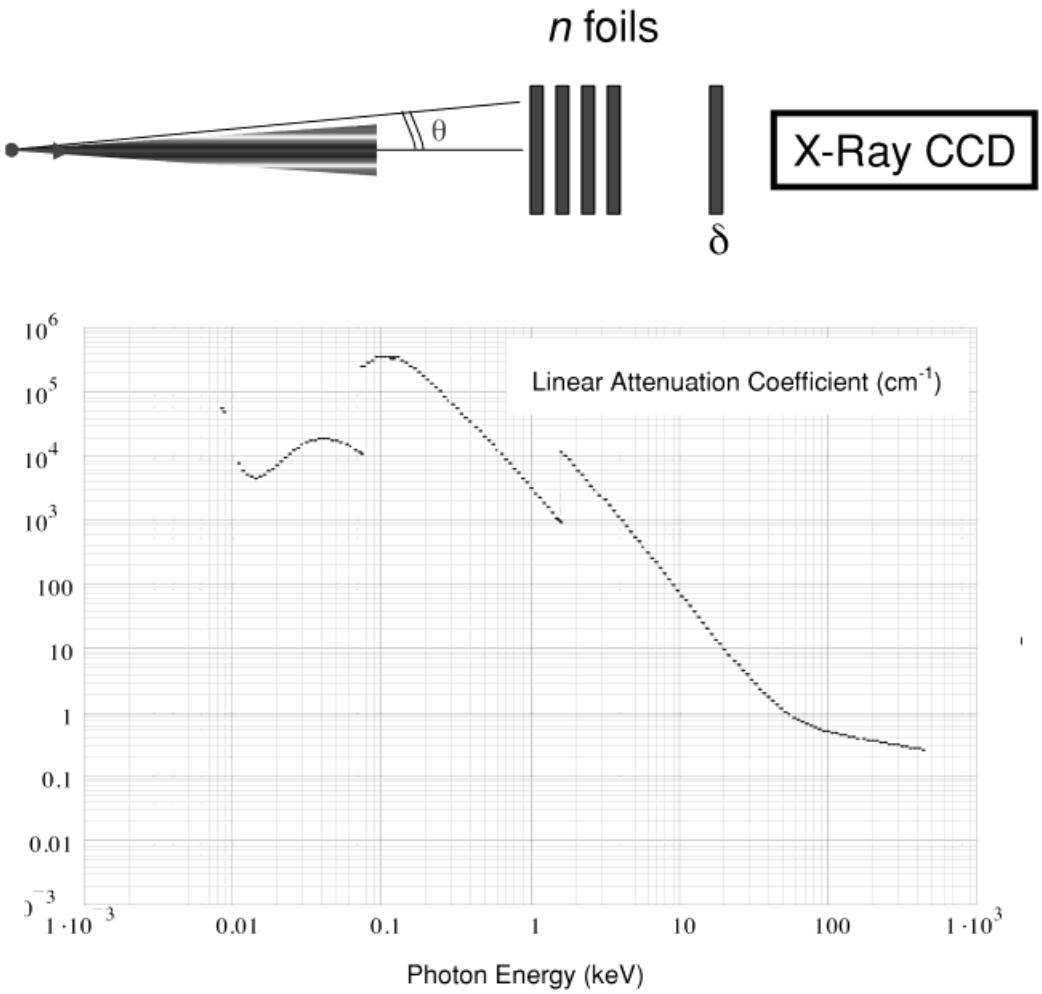

Fig. 15. Top: Illustration of the experimental procedure to measure the attenuation through calibrated foils. Bottom: Linear X-ray attenuation coefficient for Al, derived from the website at http://physics.nist.gov/PhysRefData/FFast/html/form.html.

$$T(\theta, d = n\delta) = \int_0^\infty S_x(\hbar\omega_x, \theta) \exp\left[-\frac{n\delta}{\cos\theta}\,\rho_{\mathrm{Al}}\mu_{\mathrm{Al}}(\hbar\omega_x)\right] d\hbar\omega_x, \tag{62}$$

where $S_x(\hbar\omega_x, \theta)$ is the unknown spectral energy density and n is the number of foils, of individual thickness $\delta = 787\ \mu$m. Both the density of Al and its mass attenuation coefficient are well known: $\rho_{\mathrm{Al}} = 2.70\ \mathrm{g/cm^3}$, and $\mu_{\mathrm{Al}}(\hbar\omega_x)$ is shown in Figure 15. We also note that for a small solid angle on-axis, $\cos\theta \simeq 1 - (\theta^2/2)$, and can be set equal to one in Eq. (62). To determine S_x, we introduce a trial function, consisting of a series of m steps:

$$S_x(E_x) \simeq \sum_{i=1}^{m} s_i \left\{ \mathrm{H}\left[E_x - \left(E_i - \frac{\Delta E}{2}\right)\right] - \mathrm{H}\left[E_x - \left(E_i + \frac{\Delta E}{2}\right)\right]\right\}, \tag{63}$$

where H is the unit Heaviside step-function. With this, Eq. (62) can be readily integrated, to obtain

$$T(n\delta) = \sum_{i=1}^{m} s_i \int_{E_i-(\Delta E/2)}^{E_i+(\Delta E/2)} \exp[-n\delta\rho_{\mathrm{Al}}\mu_{\mathrm{Al}}(E_x)]\,dE_x, \tag{64}$$

which can be recast as a linear system of equations, where

$$T_j = M_{i,j}\, s_j,$$

$$T_j = T(j\delta),$$

$$M_{i,j} = \int_{E_i-(\Delta E/2)}^{E_i+(\Delta E/2)} \exp[-j\delta\rho_{\mathrm{Al}}\mu_{\mathrm{Al}}(E_x)]\,dE_x. \tag{65}$$

In Eq. (65), the coefficients T_j are determined experimentally, whereas the matrix elements are derived from the well-known X-ray transmission properties of Al; the unknowns are the coefficients s_j. Provided that the number of measurements, n, is equal to the number of energy bins, m, the

https://doi.org/10.1017/S0263034604223059 Published online by Cambridge University Press

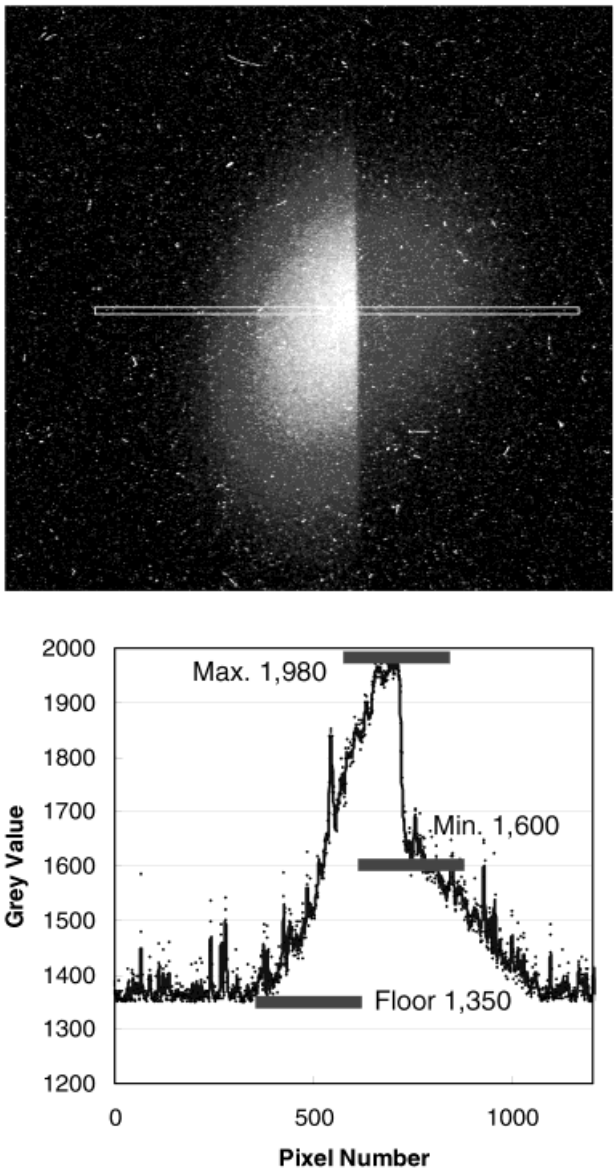

Fig. 16. Top: CCD image obtained experimentally for 15 Al foils, each 787 μm thick. Bottom: Lineout along the box shown in the top figure, and determination of the energy-integrated transmission, in this case, approximately 0.40.

system can be resolved, with the obvious caveat that the energy sampling range must reasonably map the sought-after spectrum. In practice, 9×9 systems were solved for, and it was found that only a limited set of energy binnings provided mathematically acceptable results, namely, that all the s_j coefficients be positive; moreover, all such solutions yielded spectra with very similar energy dependence. The result is shown in Figure 17, where it is compared with the theoretical prediction; the spectrum inferred from the transmission curve shown in Figure 16 is consistent with the theory. Note that as the measurements are performed with the X-ray CCD, the theoretical curve includes the transmission through BK7 and the response of the CsI scintillator.

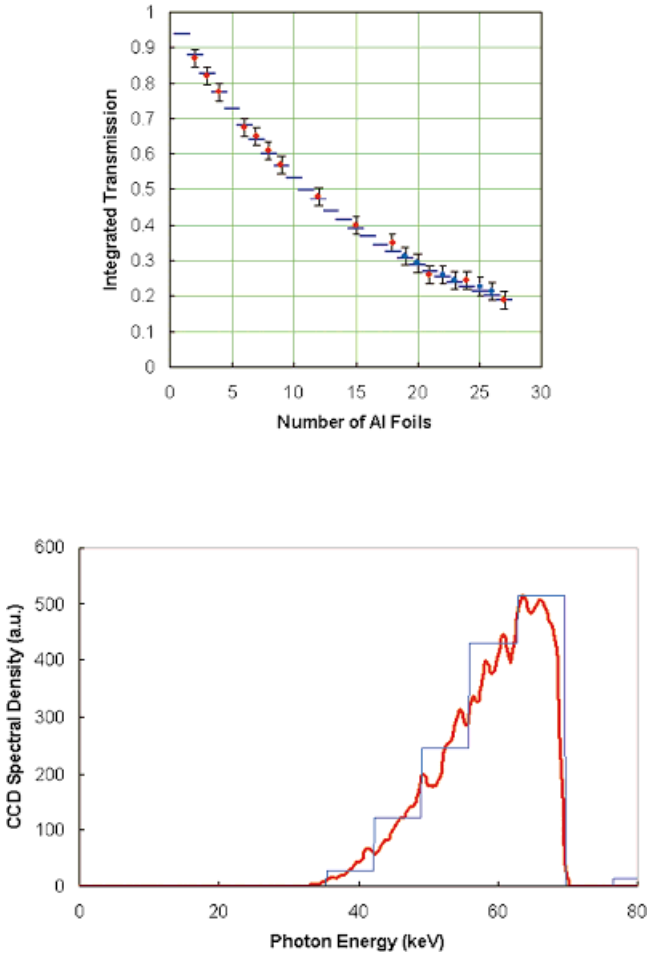

Fig. 17. Top: Energy-integrated transmission as a function of the number of Al foils; the experimental data is shown as dots with error bars; the blue horizontal lines are theoretically predicted using the frequency-domain three-dimensional code. Bottom: Theoretical spectral energy density at the CCD (red), and spectrum inferred from the transmission measurements (blue; see text). The corresponding peak brightness is $\hat{B}_x = 2.75 \times 10^{15}$ photons/(0.1% bandwidth $\times$ mrad^2 $\times$ mm^2 $\times$ s).

4.4. Peak on-axis X-ray brightness

Starting from the good inferred agreement between the three-dimensional codes and the spectral measurements, the peak brightness of the source can be evaluated as follows: The output of the three-dimensional frequency-domain code mentioned in Section 2 describes the time-integrated photon spectral density per unit frequency per unit solid angle, $d^2N_x/d\omega_x d\Omega_x$; multiplying this quantity by the photon energy, $\hbar\omega_x$, then yields the energy spectral density radiated at the source, $S_x = d^2W_x/d\omega_x d\Omega_x$. The next step consists of taking into account the transmission through the $\frac{1}{2}$-in. BK7 mirror and the 1-mm Al window, by multiplying S_x by $T_{\mathrm{BK7}}(\hbar\omega_x)T_{\mathrm{Al}}(\hbar\omega_x)$, as expressed in Eq. (58). Considering a small solid angle on-axis, $\Delta\Omega$, the total energy deposited on the corresponding area of the X-ray CCD, and properly taking into account the energy response of the CCD, as described in Eq. (56), we find that

https://doi.org/10.1017/S0263034604223059 Published online by Cambridge University Press

$$\Delta W_x = \Delta\Omega \int_0^\infty \frac{d^2N_x}{d\omega_x\, d\Omega_x} \hbar\omega_x T_{BK7}(\hbar\omega_x) T_{Al}(\hbar\omega_x) R(\hbar\omega_x^0) \times \frac{1-\exp[-\rho_{CsI}\mu_{CsI}(\hbar\omega_x)\Delta_{CsI}]}{1-\exp[-\rho_{CsI}\mu_{CsI}(\hbar\omega_x^0)\Delta_{CsI}]}\, d\omega_x. \quad (66)$$

We now consider the experimental measurement of the energy deposited on-axis in a single X-ray shot: A 6×6 pixels area registers 480 counts; as the detector is positioned 1.905 m away from the source, the corresponding solid angle is $\Delta\Omega = (6 \times 60 \times 10^{-6}/1.905)^2 = 0.036$ mrad^2. Comparing the energy density in Eq. (66) and the experimental count density, the spectrum can be used to calculate the integrated energy response on the CCD, as specified in Eq. (59); for the spectrum inferred in the previous section, this parameter is equal to 0.122 count/keV. The energy deposited is 3.94 MeV, and the integrated energy density on-axis is $dW_x/d\Omega_x = 9.69 \times 10^4$ keV/mrad^2. The number of photons per 0.1% bandwidth, per unit solid angle can now be determined by properly scaling the three-dimensional code output to match the experimental energy density: On-axis, we have

$$\frac{d^2N_x}{d\omega_x\, d\Omega_x} \times (\omega_x \times 10^{-3}) = 24.4 \text{ photons}/(0.1\% \text{ bandwidth} \times \text{mrad}^2). \quad (67)$$

At this point, we need to evaluate the source size and the X-ray pulse duration to obtain the peak brightness on-axis. To first order, the source size is simply given by the overlap integral of the electron and photon density distributions at the focus,

$$\Delta\Sigma = \int_0^\infty \exp\left(-2\frac{r^2}{w_0^2}\right)\exp\left(-\frac{r^2}{2\sigma^2}\right) 2\pi r dr = 1.19 \times 10^{-3} \text{ mm}^2, \quad (68)$$

for $w_0 = 32$ μm and $\sigma = 27$ μm rms; similarly, the temporal duration of the X-ray pulse is given by that of the electron bunch, and we have

$$\Delta t = \int_{-\infty}^\infty \exp\left(-\frac{t^2}{2\sigma_t^2}\right) dt = 7.52 \text{ ps}, \quad (69)$$

as $\sigma_t = 3$ ps rms. Finally, the on-axis peak brightness is

$$\hat{B}_x = \frac{1}{\Delta\Sigma} \times \frac{1}{\Delta t} \times \frac{d^2N_x}{d\omega_x\, d\Omega_x} \times (\omega_x \times 10^{-3}) = 2.75 \times 10^{15} \text{ photons}/(0.1\% \text{ bandwidth} \times \text{mrad}^2 \times \text{mm}^2 \times \text{s}). \quad (70)$$

This value is in good agreement with the theoretical value calculated by the three-dimensional codes.

4.5. *K*-edge radiography in tantalum

The final set of experimental data discussed in this article demonstrates the γ^2-tunability of the Compton scattering source, as well as its capability to perform radiography in high-*Z* materials, and to use the correlation between the scattering angle and the photon energy, shown in Figure 4, to detect the *K*-edge of Ta. The basic setup consists of propagating the X-ray beam through a thin foil of high-*Z* material, with a *K*-edge located near the peak of the on-axis spectrum. In the case of a 0.005-in.-thick Ta foil, where the *K*-edge lies at 67.46 keV, the results are shown in Figure 18. When the electron beam operates at 54.9 MeV, the peak of the on-axis spectrum is at 71.5 keV, just above the *K*-edge of Ta. As a result strong absorption is observed on-axis, whereas the lower energy X rays scattered off-axis are below the edge and propagate with little attenuation. The elliptical shape of the ring surrounding the on-axis hole is due to a combination of emittance and polarization effects, and is well modeled by our three-dimensional code, as shown in Figure 18. Operating the machine at 56.9 MeV pushes the peak of the on-axis spectrum to 76.7 keV, which is sufficiently far above the *K*-edge to recover some transmission: The hole fills up. Again, this is in very good agreement with the pattern predicted theoretically. Finally, a 3.6% variation in the electron beam energy yields a 7% variation in the photon energy, a clear signature of the quadratic scaling of the X-ray energy with γ.

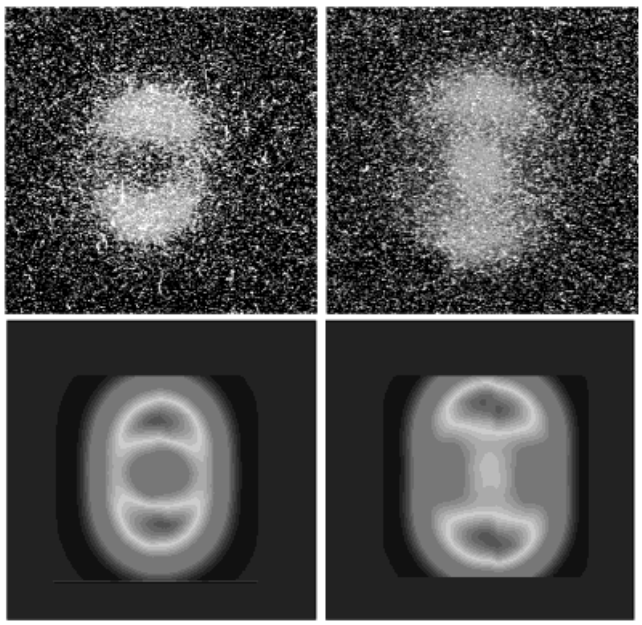

Fig. 18. Top left: Experimentally measured angular energy distribution after propagation through a 0.005-in. Ta foil, for an electron beam energy of 54.9 MeV. Bottom left: Theoretically predicted CCD response under the same conditions. Top right: Experimentally measured angular energy distribution after propagation through a 0.005-in. Ta foil, for an electron beam energy of 56.9 MeV. Bottom right: Theoretically predicted CCD response under identical conditions.

https://doi.org/10.1017/S0263034604223059 Published online by Cambridge University Press

5. CONCLUSIONS AND FUTURE EXPERIMENTAL PROGRAM

To date, we have demonstrated successful Compton scattering in the 180° geometry, and observed X-ray fluxes and beam profiles that agree well with the theoretically predicted values. The next steps are to confirm the experimentally inferred on-axis spectrum and to measure the spectrum as a function of the scattering angle. This will be done using an XR-100CR X-ray diode as well as LiF crystals. These measurements, together with source size measurements and the use of an X-ray streak camera at lower energies, will allow us to verify the spectral brightness. Lower backgrounds will also be pursued, using the techniques outlined in Section 4.3.

According to theory, the X-ray flux can still be increased by two orders of magnitude by operating at full electron bunch charge, at 1 nC instead of 266 pC, and by using a new set of permanent magnet quadrupoles (PMQs) designed and assembled at the University of California, Los Angeles. These new quadrupoles provide up to 300 T/m of focusing gradient, as compared to 15–20 T/m for the current electron beam optics; the rms spot radius resulting from the proper tuning of the PMQs has been modeled theoretically and is estimated to be in the 5–10 μm range. Furthermore, the peak brightness can be increased by one order of magnitude using velocity compression on the electron bunch. This technique has been demonstrated at PLEIADES, and electron bunch durations below 300 fs rms have been obtained; collisions with the FALCON laser pulse have also produced X rays, with doses comparable to those described here for uncompressed bunches. In that case the inferred peak photon flux approaches 10^{19} photons/s, which represents a very high number for 70 keV X rays.

A series of ultrafast Bragg diffraction experiments on high-Z materials, with the goal of studying linear and nonlinear phonon modes as well as nonthermal melting and laser-induced phase transitions, will be performed in the near future.

Finally, the nonlinear regime, where the normalized vector potential, A_0, exceeds unity, will be studied experimentally by using a lower f-number off-axis parabola. In this regime, for circularly polarized light, one can take advantage of the $1/(1 + A_0^2)$ downshift induced by radiation pressure to increase the electron beam energy to maintain the X-ray energy, $\hbar\omega_x = \hbar\omega_0 4\gamma^2/(1 + A_0^2)$, constant, thus decreasing the natural emittance of the beam, ε_n/γ. It can be shown that the X-ray brightness scales as $\gamma^2/\varepsilon_n^2 \propto (1 + A_0^2)/\varepsilon_n^2$; thus extremely high brightness could be reached with modest laser energies, as the source size would nearly match the diffraction-limit of the laser.

ACKNOWLEDGMENTS

This work was performed under the auspices of the U.S. Department of Energy by the University of California, Lawrence Livermore National Laboratory under Contract W-7405-Eng-48. UCRL-JP-200521.

REFERENCE

Arthur, J., Materlik, G., Tatchyn, R. & Winick, H. (1995). *Rev. Sci. Instrum.* **66**, 1987.

Banber, C., Boege, S.J., Koffas, T., Melissinos, A.C., Meyerhofer, D.D., Reis, D.A., Ragg, W., Bula, C., McDonald, K.T., Prebys, E.J., Burke, D.L., Field, R.C., Horton-Smith, G., Spencer, J.E., Walz, D., Berridge, S.C., Bugg, W.M., Shmakov, K. & Weidemann, A.W. (1999). *Phys. Rev. D* **60**, 092004/1–43.

Barty, C.P.J., Guo, T., Le Blanc, C., Raksi, F., Rose-Petruck, C., Squier, J., Wilson, K.R., Yakovlev, V.V. & Yamakawa, K. (1996). *Opt. Lett.* **21**, 668.

Biedron, S.G., Goeppner, G.A., Lewellen, J.W., Milton, S.V., Nassiri, A., Travish, G., Wang, X.J., Arnold, N.D., Berg, W.J., Bazbien, M., Doose, C.L., Dortwegt, R.J., Grelick, A., Galayda, J.N., Markovich, G.M., Pasky, S.J., Power, J.G. & Yang, B.X. (1999). *Proc. Particle Accelerator Conference 1999*, 2024.

Bula, C., McDonald, K.T., Prebys, E.J., Bamber, C., Boege, S., Kotseroglou, T., Melissinos, A.C., Meyerhofer, D.D., Ragg, W., Burke, D.L., Field, R.D., Horton-Smith, G., Odian, A.C., Spencer, J.E., Walz, D., Berridge, S.C., Bugg, W.M., Shmakov, K. & Weidemann, A.W. (1996). *Phys. Rev. Lett.* **76**, 3116.

Burke, D.L., Field, R.C., Horton-Smith, G., Odian, A.C., Spencer, J.E., Walz, D., Berridge, S.C., Bugg, W.M., Shmakov, K., Weidemann, A.W., Bula, C., McDonald, K.T., Prebys, E.J., Bamber, C., Boege, S., Kotseroglou, T., Melissinos, A.D., Meyerhofer, D.D., Reis, D.A. & Ragg, W. (1997). *Phys. Rev. Lett.* **79**, 1626.

Carlsten, B.E. (1989). *Nucl. Instrum. Methods Phys. Res. A* **285**, 313–319.

Cavalleri, A., Siders, C.W., Brown, F.L.H., Leitner, D.M., Toth, C., Squier, J.A., Barty, C.P.J., Wilson, K.R., Sokolowski-Tinten, K., Horn von Hoegen, M., von der Linde, D. & Kammler, M. (2000). *Phys. Rev. Lett.* **85**, 586.

Chin, A.H., Schoenlein, R.W., Glover, T.E., Balling, P., Leemans, W.P. & Shank, C.V. (1999). *Phys. Rev. Lett.* **83**, 336.

Dirac, P.A.M. (1938). *Proc. Roy. Soc. London, Ser. A* **167**, 148.

Esarey, E., Ride, S.K. & Sprangle, P. (1993). *Phys. Rev. E* **48**, 3003–3021.

Esarey, E., Sprangle, P. & Krall, J. (1995). *Phys. Rev. E* **52**, 5443–5453.

Fitzgerald, R. (2000). *Phys. Today* **53**, 23.

Fultz, S.C. & Whitten, C.L. (1971). *IEEE Trans. Nucl. Sci.* **18**, 533.

Gradshteyn, I.S. & Ryzhik, I.M. (1980). *Table of Integrals, Series, and Products*, 4th Ed., Orlando, FL: Academic Press.

Greiner, W. & Reinhardt, J. (1994). *Quantum Electrodynamics*. Berlin: Springer Verlag.

Guo, T., Spielmann, Ch., Walker, B.C. & Barty, C.P.J. (2001). *Rev. Sci. Inst.* **72**, 41.

Hartemann, F.V. (1998). *Phys. Plasmas* **5**, 2037–2047.

Hartemann, F.V. (2000). *Phys. Rev. E* **61**, 972–975.

https://doi.org/10.1017/S0263034604223059 Published online by Cambridge University Press

Hartemann, F.V. (2002). *High Field Electrodymanics.* Boca Raton, FL: CRC Press.

Hartemann, F.V., Baldis, H.A., KIerman, A.K., Le Foll, A., Luhmann, N.C., Jr. & Rupp, B. (2001). *Phys. Rev. E* **64**, 016501.

Hartemann, F.V. & Kerman, A.K. (1996). *Phys. Rev. Lett.* **76**, 624–627.

Hartemann, F.V., Van Meter, J.R., Troha, A.L., Landahl, E.C., Luhmann, N.C. Jr., Baldis, H.A. Gupta, A. & Kerman, A.K. (1996). *Phys. Rev. E* **54**, 2956–2962.

Hartemann, F.V., Troha, A.L., Luhmann, N.C. Jr. & Toffano, Z. (1998). *Phys. Rev. E* **58**, 5001.

Hogan, M.J., Pellegrini, C., Rosenzweig, J., Anderson, S., Frigola, P., Tremaine, A., Fortgang, C., Nguyen, D.C., Sheffield, R.L., Kinross-Wright, J., Varfolomeev, A., Varfolomeev, A.A., Tolmachev, S. & Carr, R. (1998). *Phys. Rev. Lett.* **81**, 4867–4870.

Lawson, W., Bellamy, C. & Brosuis, D.F. (Eds.). (1999). *Advanced Accelerator Concepts, 8th Workshop,* Conference Proceedings No. 472. Woodbury, NY: American Institute of Physics.

Le Sage, G.P., Anderson, S.G., Cowan, T.E., Crane, J.K., Dimire, T. & Rosenzweig, J.B. (2001). *Proc Ninth Workshop on Anvanced Accelerator Concepts* Colestock, P.L. & Kelley, S., Eds.), Vol. 569, p. 391. American Institute of Physics.

Leemans, W.P., Schoenlein, R.W., Volfbeyn, P., Chin, A.H., Glover, T.E., Balling, P., Zolotorev, M., Kim, K.J., Chattopadhyay, S. & Shank, C.V. (1996). *Phys. Rev. Lett.* **77**, 4182.

Leemans, W.P., Schoenlein, R.W., Volfbeyn, P., Chin, A.H., Glover, T.E., Balling, P., Zolotorev, M., Kim, K.J., Chattopadhyay, S. & Shank, C.V. (1997). *IEEE Journal of Quantum Electronics* **33**, No. 11 1925, 1997.

Lindenberg, A.M., Kang, I., Johnson, S.L., Missalla, T., Heimann, P.A., Chang, Z., Larsson, J., Bucksbaum, P.H., Kapteyn, H.C., Padmore, H.A., Lee, R.W., Mark, J.S. & Falcone, R.W. (2000). *Phys. Rev. Lett.* **84**, 111.

Litvinenko, V.N., Burnham, B., Emamian, M., Hower, N., Madey, J.M.J., Morcombe, P., O'Shea, P.G., Park, S.H., Sachtschale, R., Straub, K.D., Swift, G., Wang, P., Wu, Y., Canon, R.S., Howell, C.R., Roberson, N.R., Schreiber, E.C., Spraker, M., Tornow, W., Weller, H.R., Pinayev, I.V., Gavrilov, N.G., Fedotov, M.G., Kulinapov, G.N., Yurkin, G.Y., Mikhailov, S.F., Popik, V.M., Skrinsky, A.N., Vinokurov, N.A., Norum, B.E., Lumpkin, A. & Yang, B. (1997). *Phys. Rev. Lett.* **78**, 4569.

Mourou, G.A., Barty, C.P.J. & Perry, M.D. (1998). *Phys. Today* **51**, 22–28.

O'Shea, P., Kimmel, M., Gu, X. & Trebino, R. (2001). *Opt. Lett.* **26**, 932.

O'Shea, P., Kimmel, M. & Trebino, R. (2002). *J. Opt. B* **4**, 44.

Perry, M.D. & Mourou, G. (1994). *Science* **264**, 917–924.

Reiser, M. (1994). *Theory and Design of Charged Particle Beams.* New York: John Wiley and Sons.

Ride, S.K., Esarey, E. & Baine, M. (1995). *Phys. Rev. E* **52**, 5425–5442.

Robb, R.A. (1995). *Three-dimensional Biomedical Imaging: Principles & Practice*. New York: Wiley-VCH Publishers.

Roberson, C.W. & Sprangle, P. (1989). *Phys. Fluids B* **1**, 3.

Rose-Petruck, C. et al. (1999). *Nature* **398**, 310.

Schoenlein, R.W., Chattopadhyay, S., Chong, H.H.W., Glover, T.E., Heimann, P.A., Shank, C.V., Zholents, A.A. & Zolotorev, M.S. (2000). *Science* **287**, 2237.

Schoenlein, R.W., Leemans, W.P., Chin, A.H., Volfbeyn, P., Glover, T.E., Balling, P., Zolotorev, M., Kim, K.-J., Chattopadhyay, S. & Shank. C.V. (1996). *Science* **274**, 236–238.

Siders, C.W., Cavalleri, A., Sokolowski-Tinten, K., Tost, C., Guo, T., Kammler, M., Horn von Hoegen, M., Wilson, K.R., von der Linde, D. & Barty, C.P. J. (1999). *Science* **286**, 1340.

Umstadter, D.P., Barty, C., Perry, M & Mourou, G.A. (1998). *Opt. Phot. News* **9**, 41.

Wiedemann, H. (1999). *Particle Accelerator Physics*, 2nd Ed., Vol. 1, New York: Springer.

Yu, D., Newsham, D., Wilson, P., Zeng, J., Rosenzweig, J., Ding, X., Hartemann, F. & Landahl, E. (1999). In: *Proc. Particle Accelerator Conference 1999*, 2003.

Zholents, A.A. & Zolotorev, M.S. (1996). *Phys. Rev. Lett.* **76**, 912.